Microstructural analysis and thermomechanical testing of nickel thin films

Aidan Taylor

Jahnstraße 12, A–8700 Leoben, Austria

June 2008

Abstract

The microstructure and thermomechanical properties of Ni thin films were investigated by a range of techniques. The films were $150 - 1000nm$ thick and were sputter-deposited onto both oxidised Si (100) and α-Al_2O_3 (0001) substrates. The films deposited onto Si wafers formed a {111}–textured columnar microstructure with a mean grain size similar to the film thickness while those on α-Al_2O_3 formed an epitaxial microstructure with two broad, twin-related, alignments with the substrate. Thermomechanical testing with a wafer curvature apparatus indicated that the yield stress of the polycrystalline films increased with decreasing film thickness until a plateau of ~1100 MPa was reached, this plateau is attributed to the present experiments exerting insufficient thermal strain to induce yielding in the thinner films. At elevated temperatures the compressive yield in the films shows a competition between dislocation and diffusion controlled plasticity. The room temperature and elevated temperature yield for the epitaxial films increased with decreasing film thickness, showing good quantitative agreement with the Nix-Freund model.

June 2008 Univ. Prof. Dr. Gerhard Dehm

Declaration

I declare that all the work contained herein is my own except where otherwise noted and that I have applied work found in the literature only where duly noted.

Acknowledgments

First and foremost I would like to thank Professor Dehm for all the help and advice in completing this manuscript as well as for the assistance he has given me with the TEM. In addition I would like to thank both Gabi Moser and Natascha Sauer for their help in producing samples for electron microscopy. Finally, I would like to thank Dr. Stewart, Dr. Chasty, all the nurses in Ward 117 at Staffordshire County General and the past 20 years of oncology research for giving me the opportunity to do this.

Contents

1 Introduction **7**

2 Literature Review **9**

2.1 Microstructure . . . 9

2.2 Theoretical Approaches to Wafer Curvature . . . 11

2.3 Experimental Approaches to Wafer Curvature . . . 15

3 Experimental Procedure **17**

3.1 Film Deposition . . . 17

3.2 Microstructural Characterisation . . . 18

3.3 Wafer Curvature . . . 20

4 Results **23**

4.1 Microstructure . . . 23

4.1.1 Polycrystalline Films . . . 23

4.1.2 Epitaxial Films . . . 29

4.2 Wafer Curvature . . . 34

4.2.1 Polycrystalline Films . . . 34

4.2.2 Epitaxial Films . . . 42

4.2.3 Thermomechanical Gradients . . . 44

5 Discussion **47**

5.1 Microstructure . . . 47

5.2 Wafer Curvature . . . 49

6 Summary **55**

References **56**

A TEM Sample Preparation **58**

B Experimental errors in wafer curvature measurement **59**

C Microstructural Data **61**

C.1 Representative FIB micrographs 61

C.1.1 1000nm film on SiN_x/SiO_x 62

C.1.2 600nm film on SiN_x/SiO_x 62

C.1.3 400nm film on SiN_x/SiO_x 63

C.1.4 200nm film on SiN_x/SiO_x 63

C.1.5 150nm film on SiN_x/SiO_x 64

C.2 Grain count statistics 64

C.3 EBSD Data 66

C.3.1 1000nm film on α-Al_2O_3 67

C.3.2 600nm film on α-Al_2O_3 68

C.3.3 400nm film on α-Al_2O_3 69

C.3.4 200nm film on α-Al_2O_3 70

D Wafer curvature data **70**

D.1 Polycrystalline Films 71

D.2 Epitaxial Films 73

1 Introduction

As devices such as microprocessors, their associated electronics, as well as micro-electromechanical systems reduce in size and become more complex the individual features in their construction enter the nanometer scale. The latest generation of Intel microprocessors, Penryn, has a feature size of just $45nm$. It is however known [1] that metals, such as those used in the metallisation lines of said devices, do not behave in the same way on this sub-micron size scale as a scaling-down of bulk mechanical properties would predict. In particular, metals regularly exhibit a higher yield stress when tested in very small dimensions, eg. [2, 3, 4, 5], more so than predicted by the Hall-Petch relation [6, 7].

There are in fact two components to the investigation of thin films in this manner; the microstructure and the thermomechanical properties. The microstructure of thin metallic films depends on many factors, including deposition temperature, film substrate and film thickness, and so it is important to have a thorough understanding of this prior to any investigation of the thermomechanical properties.

Previous work has suggested that fcc metallic thin films on an amorphous substrate have a preferred texture as well as a linear relation between film thickness and grain size [3, 4]. In addition to this, crystalline substrates can lead to quite different microstructures due to epitaxy at the interface. These effects are important in the nanotechnology industry as metallisation is deposited on a variety of substrates including Si, GaN and GaAs as well as α-Al_2O_3 and amorphous substrates. Control, predictability and understanding of the microstructure is an important concern as it effects the electrical and diffusion properties of the metallisation in addition to the mechanical properties. In this study oxidised Si, providing an

amorphous surface, and α-Al_2O_3 substrates were used to provide a combination of an idealised system in addition to a system more representative of what is seen in industrial applications.

Due to the mismatch in thermal expansivity between these metal thin films and the substrates onto which they are deposited it is very common for large stresses to be present in the films. This is often made worse by the repeated thermal cycling of a component, such as a microprocessor, during manufacture and use. The high stresses in these films, combined with the modification in their mechanical properties compared to bulk materials, can lead to the unpredicted failure of these devices [8]. It is therefore important to advance understanding in these fields such that these small-scale mechanical properties of metals are better understood, this understanding will then lead to future design in which the technology can continue to advance without an increased risk of failure.

Several methods exist for the measurement of stresses in films on a substrate. These revolve around four principal techniques, measuring either the radius of curvature caused by differential thermal expansion between film and substrate or they more directly measure the change in lattice parameters of the film to assess the strain directly. In this study the measurements of stress in the film were carried out using a laser to measure the curvature of the film and substrate as outlined by Nix [9]. The other techniques for assessing film stress are interferometry, capacitance and x-ray diffraction [10].

Theoretical models have been proposed to determine the physical processes taking place in the metal films during thermomechanical testing. These models aim to recreate the stress-temperature cycles exhibited by the metal films through physical modelling of the dislocation and diffusion phenomena controlling the film

properties. In particular, the Nix-Freund model [1, 11] of dislocation glide on inclined planes and Gao's model [12, 13] of constrained diffusional creep have shown considerable success at producing quantitative agreement between experiment and theory.

2 Literature Review

2.1 Microstructure

There are several factors that can affect the microstructure of metallic thin films, these include, but not exhaustively; film thickness, deposition temperature and deposition rate, substrate material and the presence of post treatments such as annealing. In this study the film thickness and film substrate were varied, as such the literature relevant to these factors is presented here.

The work of Westmacott et al. [14] has shown that thin films of many different metals, fcc as well as other structures, can be grown epitaxially on single crystal substrates. It was found that the epitaxial alignment could result in bicrystals and tricrystals in addition to single crystals, this was due to rotational symmetry of the epitaxial alignment with respect to the interface. It was also found that the nature of the epitaxy depended on the deposition temperature for many systems. Subsequent work with fcc metals on α-Al_2O_3 has found that a bicrystal epitaxy is common with either $\{111\}\pm<\bar{1}10>$fcc//(0001)$<10\bar{1}0>$ α-Al_2O_3 (OR1) or $\{111\}\pm<11\bar{2}>$fcc//(0001)$<10\bar{1}0>$ α-Al_2O_3 (OR2) alignment [3].

On an amorphous substrate the microstructure of the deposited metal is controlled by surface and strain energy considerations. The theoretical work of Thomp-

son and Carel [15] suggests that fcc metals will have a {111} fibre texture parallel to the interface for very thin films as the low surface energies of the close packed planes at the surface and interface dominate the energetics. As the film increases in thickness the effect of the strain energy stored in the film becomes increasingly important. This strain energy is due to thermal mismatch between the film and substrate and it favours the {100} fibre texture as these planes have the lowest biaxial modulus. Storage of strain energy is given as follows:

$$U_\epsilon = \sigma\epsilon = M_{hkl}\epsilon^2 \tag{1}$$

Where U_ϵ is the elastic strain energy, ϵ is strain, σ is stress and M_{hkl} is the biaxial modulus for the relevant planes (hkl). As such, Thompson and Carel predicted a crossover in the texture from a {111} fibre texture for thinner films to a{100} texture past a critical thickness, h_c, dependent upon the difference in surface energies and biaxial moduli of the {111} and {100} planes. Experimental support for this theory was produced by Sonnweber-Ribic et al. [16] through texture analysis of Cu films on polyimide substrates. In this case a transition occurs between 3 and 5 μm. This value is dependent upon the metal, substrate and deposition conditions but it is likely that h_c is found at the same order of magnitude for the Ni/Si system investigated here.

The work of Mullins [17] for columnar grains in unconstrained sheets produces a theory for the relation between sheet thickness and the size of the grains due to the grain boundary pinning effect of thermal grooving. In this model a grain size a little larger than the sheet thickness is predicted, if the if the sheet can only groove on one surface however then a value of 1.5-2 times the film thickness is predicted.

Previous work for fcc metal films deposited under similar conditions have produced columnar grains on both the Si and α-Al_2O_3 substrates [3, 4]. In these studies the metals deposited onto the amorphous, $SiN_x/SiO_x/Si$, substrate exhibit a {111} fibre texture of log-normally distributed grain sizes whose mean size is 1.0-1.5x the film thickness. The metal deposited onto the α-Al_2O_3 substrate produced mixed results. Both OR1 and OR2 orientation relations were found for the various fcc metals but the sharpness of the epitaxy varied significantly, in some cases the microstructure was closer to a {111} fibre texture than true bicrystal epitaxy.

In assessing the microstructure of thin metal films, focussed ion beam (FIB) imaging is very useful as the high channeling contrast [18] the technique provides allows high confidence distinction of grain boundaries and hence good grain count statistics. The work of Atwater et al. [19, 20] has however produced strong evidence that preferentially oriented grains experience growth to the detriment of their neighbours during FIB exposure. This suggests that the grain counts performed in this way can overestimate the true grain size present in the material.

2.2 Theoretical Approaches to Wafer Curvature

When performing radius of curvature measurements for thin films on a substrate the thin film approximation [21] is essential for converting curvature into film stress, σ_f. This work suggests that if the film is at least 100 times thinner than the substrate then the following equation is applicable:

$$\sigma_f = \frac{M_s h_s^2}{6h_f}\Delta K \qquad (2)$$

Here M_s is the biaxial modulus of the substrate, h_s is the substrate thickness and h_f is the film thickness. ΔK is the change in curvature due to the film stress. This is very useful as it allows for determination of the film stress without explicit knowledge of any of the film properties other than the thickness.

Among the theoretical approaches to understanding the form of the stress-temperature curves produced by this technique the work presented here will focus on Nix [1] and Freund's [11] model of dislocation glide on inclined planes in thin films as well as Gao's [12] description of constrained diffusional creep in thin films at elevated temperatures. The Nix–Freund model is only truely applicable to single crystal films as grain boundaries were not accounted for in this model, as such the theory of von Blanckenhagen *et al.* [22] is also considered as this work uses simulation to predict the shear stresses necessary to activate Frank–Read sources within a grain.

The Nix-Freund model describes dislocation glide on planes inclined to the substrate. No allowance is made in this model for grain boundaries and so quantitative agreement is only a realistic possibility for the single crystal films on α-Al_2O_3. It has however been found in several studies [3, 5, 4] that the stress in polycrystalline films of different thicknesses also correlates well in a qualitative manner with the Nix-Freund model, ie. a linear relation can be found in a plot of film stress against inverse thickness. The following relation is predicted [1]:

$$\sigma_y = \frac{\sin\varphi}{\cos\varphi\cos\lambda}\frac{b}{4\pi(1-\nu)h_f)}\left(\mu_{eff}\ln\left[\frac{\beta_s}{b}h_f\right]\right) \quad (3)$$

where φ is the angle between the film normal and the inclined slip planes, λ is the angle between the film normal and the Burger's vector, b, ν_f the Poisson's

ratio of the film and β_s is a numerical constant, of value 1-2, defining the cut-off ratio of the stress field of the interfacial dislocation. The effective shear modulus, μ_{eff}, takes the interaction of the dislocation with both the film and the substrate into account.

The model proposed by Gao et al [12] for constrained diffusional creep assumes that polycrystalline films at high temperatures relax stresses via surface diffusion from the centre of the grains to the grain boundaries. As such this model predicts greater degrees of relaxation for thinner films with a larger surface-to-volume ratio. The relation links the flow stress at elevated temperatures to the film thickness and grain size as follows [12]:

$$\sigma_f = \sigma_{el} - (\sigma_{el} - \sigma_{gb}) \left(\frac{4h_f}{d} \tanh \left[\frac{d}{4h_f} \right] \right) \tag{4}$$

where σ_{el} is the stress induced due to thermal mismatch, d is the grain size and σ_{gb} is the grain boundary traction. The grain boundary traction is given by:

$$\sigma_{gb} = \sigma_{el} \exp \left(-\frac{\lambda t}{t_0} \right) \tag{5}$$

where t is the time and λ is a constant whose value is a function of the film thickness to grain size ratio. t_0 is a characeristic time expressed by:

$$t_0 = \frac{4k_B T h_f^3}{M_{hkl} \delta D_{gb} \Omega} \tag{6}$$

In this relation, M_{hkl} is the plane-strain elastic modulus of the film, k_B is Boltzmann's constant, δ is the grain boundary width, Ω is the atomic volume and D_{gb} is the grain boundary diffusivity.

Weiss et al. [13] went on to apply this theoretical approach such that simulated stress-temperature plots were produced for polycrystalline films. This work produced simulated cycles for both unpassivated Cu and passivated Cu films assuming that thermally activated dislocation glide and constrained diffusional creep were the only mechanisms of plastic deformation, for the passivated films it was assumed that diffusional flow was completely suppressed. The passivated Cu films contained around 1% Al such that a passivating oxide is formed on the film surface and hence any diffusional flow along the film surface is suppressed. The simulated curves reproduced many of the features present in the cycles for both types of film, although it should be noted that parameters such as the grain size and activation energies were chosen such that the theory approached the experimental values.

Von Blanckenhagen *et al.* [22] used computer simulation to determine the shear stresses involved in the activation of Frank–Read sources in a polycrystalline film. This work made several assumptions in the modelling; dislocations could not escape the grain at any boundary, only one source was active, this source was positioned in the centre of the grain and glide occurred on an inclined {111} with the most favourable Burger's vector. These parameters ensure that the modelling will produce a lower bound for the stresses involved. By modelling different grain and Frank–Read source geometries von Blanckenhagen *et al.* found several key results. The first of these was that the shear stress required to activate the source, τ^*, was dependent on whichever was smaller of the grain size and the film thickness. Secondly they found that repeated activation of the source led to large back-stresses in the grain and hence activation of the source rapidly becomes more difficult. Finally they found that their model predicted a flow stress in the film to be at least three times higher than that predicted by the Nix–Freund model. Comparison of

this prediction with data for Cu tests found very promising agreement, particularly once grain size was taken into account in addition to film thickness.

From this work the following relation was produced:

$$\tau^* \approx \frac{\mu b}{s_{eff}} \tag{7}$$

Where s_{eff} is the effective size of the Frank–Read source, this is at its minimum for $h_f/3$ (or $d/3$ depending on which is smaller.)

2.3 Experimental Approaches to Wafer Curvature

There are several experimental studies of metallic thin films relevant to the work presented here. Face centered cubic metals have been the subject of most studies; Ag [2, 23], Cu [3, 4, 13] and Al [24, 3, 25] while Wellner [5, 26] studied the NiAl intermetallic. The work of Eiper *et al.* was carried out using diffraction techniques to determine film stresses, all the other studies made use of wafer curvature and *in situ* testing.

The work of Kobrinsky *et al.* [2, 23] focussed on *in situ* observation of dislocations and their glide. Using this data the activation volume for the dislocations could be determined. They concluded that the small activation volumes observed were indicative of thermally activated dislocation glide in these polycrystalline films, this was somewhat in contradiction to the channelling dislocations predicted by the Nix–Freund model. Their *in situ* observations showed that the distance between pinning points in these films decreased with film thickness providing a possible cause of the size dependence in the ambient temperature flow stresses recorded for the films.

Dehm *et al.* used α-Al_2O_3 substrates to produce epitaxial Al and Cu films such that the Nix–Freund model could be tested more correctly. Good quantitative agreement was achieved between these epitaxial films and the Nix–Freund model.

Balk *et al.* [4] observed dislocations gliding parallel to the film/substrate interface in Cu films during *in situ* thermal straining. As there should not be a shear stress resolved in this direction this result was taken to be a strong indication of the constrained diffusional creep proposed by Gao *et al.* [12]. This is because the 'diffusion wedges' at grain boundaries proposed by this model lead to a highly inhomgeneous stress distribution in the film, thus allowing for resolved shear stresses parallel to the interface.

Wellner [26] observed that the gradient of the thermoelastic portion of the stress-temperature cycles was also a function of film thickness. Wellner attributed this variation to local dislocation plasticity, i.e. thinner films contain fewer large grains in which limited plasticity is possible and hence the thermoelastic slope approaches that dictated by the thermal mismatch between film and substrate. Wellner also found that the high temperature flow stress of the films showed a competition between two mechanisms. A maximum was observed for $800nm$ films while the value reduced for both thicker, up to $3000nm$, and thinner, down to $200nm$, films. Wellner attributed this to a competition between dislocation mediated plasticity for thicker films and grain boundary diffusion for thinner films.

In the work of Dehm, Balk, Kobrinsky and Wellner a plateau in the room temperature flow stress is observed in which the stress ceases to rise below $h_f \approx 400nm$. Eiper *et al.* [25] investigated the flow stress in the Al films, previously studied by Dehm et al. [3], at cryogenic temperatures. They found that the flow stresses in the thicker films remained stable while those of sub-$600nm$ thickness

rose significantly as the temperature was further reduced. This strongly indicates that the stress plateau is a product of the thermal strain being insufficient to cause true flow in these films; if we could induce a sufficiently large strain in these films it is possible that the dependence on inverse film thickness would continue for the thinner films.

The study of Ni films in the present work aims to further the knowledge of face centered cubic metal thin film microstructure and properties and to compare the results to known models.

3 Experimental Procedure

3.1 Film Deposition [1]

The films examined in this study were produced by magnetron sputtering onto (0001)-oriented α-Al_2O_3 (50mm diameter, 330μm thickness) in the case of the epitaxial films while the polycrystalline films were deposited onto (001)-oriented Si wafers (50mm diameter, 280μm thickness). The Si substrates were coated with a 100nm amorphous-SiN_x/amorphous-SiO_x (SiN_x/SiO_x) bilayer such that interdiffusion between metal and substrate is inhibited while an amorphous surface for deposition is produced. The substrates were mounted in an ultrahigh vacuum (UHV) deposition system where they were Ar^+ sputter-cleaned (10^{-2} Pa Argon pressure, $100-500eV$ kinetic energy) to remove surface contaminants. Film deposition was achieved using a magnetron sputtering system (DCA Instruments) with a base pressure of $\sim 10^{-8}$ Pa. Prior to sputtering the 99.999% purity Ni target was

[1] All films were deposited at the Max Planck Institute for Metals Research (Stuttgart).

degassed by pre-sputtering. All the films were deposited at $100°C$ with a UHV compatible magnetron source (Mighty Mak) in 99.9999% pure Ar. The epitaxial films were deposited at $0.2Pa$ while the polycrystalline films were deposited at a pressure of 0.5 Pa, the deposition rate for both substrates was $\sim 1.1nms^{-1}$. Following deposition the films were annealed at $600°C$ for 15 min in the vacuum chamber such that contamination was avoided and a stable microstructure was produced. The films were then cooled as rapidly as the apparatus would allow by switching off the substrate heater.

3.2 Microstructural Characterisation

The microstructures of the films were evaluated by several techniques. The films on Si wafers were primarily analysed with a focussed ion beam microscope (FIB, FEI 200 at $30kV$), the channelling contrast that this provided allowed accurate distinction of grains. In addition, all images were acquired at 0, 15 and 25° so that distinction of grain boundaries could be confident. The grain area technique was used to determine the grain size distribution by manually tracing the grain boundaries onto transparent plastic and then using a grain counting system (Leica, Quantimet Q500/W). With this system the area of each grain is determined and a grain diameter for a circle of equivalent area is calculated, this grain diameter is then used for the statistical analysis. Twin boundaries were disregarded in this analysis. In addition, the FIB was used to cut out a trench in each of the films such that the film thickness and cross-sectional microstructure could be assessed to some degree.

The second technique used for microstructural analysis was electron backscatter

diffraction (EBSD), this was used in the characterisation of the films on α-Al_2O_3. For this technique a field emission gun scanning electron microscope (FEG-SEM, LEO 1525) was used with an EBSD camera (EDAX) attached such that the local crystallographic alignment is determined. Several different plots were then produced with the data. The software produced pole figures by plotting each data point on a stereographic projection, the alignment of which is user defined; this allowed evaluation of the extent to which the films had grown epitaxially. By defining a minimum angular misorientation to constitute a grain boundary the software can also produce plots in which each 'grain' is uniquely coloured, allowing for diagrams in which individual grains are easily discernible. By defining different angular limits allowable within a grain these plots can either map out the two broad orientation variations or, with a low allowable variation, the substructure of low angle boundaries can be assessed. Finally, plots were produced by the software in which the quality of the Kikuchi pattern on the camera is plotted as a grey-scale. This representation of the data gives a further means of assessing the substructure [27] as the meeting of grains, even those of very similar orientation, degrades the Kikuchi pattern. This is caused by grooving of the surface and blurring of the pattern due to the angular difference.

In addition to these techniques for determining the grain size of the films several other techniques were used for texture analysis and more in-depth microstructural studies. The first of these was x-ray diffraction (XRD). XRD was used to take pole figures of the films on Si wafers, this then allows an insight into the texture of the films. By setting the 2θ as the $\{111\}$ reflection the pole figure gives a quantitative analysis of how parallel the $\{111\}$ planes are to the substrate, if any other crystallographic planes tend to lie parallel to the substrate and if there is

any preferred orientation of the {111} planes on the substrate surface.

For the further microstructural analysis transmission electron microscopy (TEM, JEOL 2000FX at $200kV$) was used with a plan view sample geometry. For details of the sample preparation method and sample geometry refer to appendix A. This sample geometry allows for *in situ* stress-temperature experiments to be performed using a heating stage to take the sample up to about $500°C$ while a high-speed CCD camera, 25 frames/s, records video footage of the electron transparent region [4]. A further advantage of this preparation method is that it affords a large electron-transparent region from which further grain size analysis may be conducted. This was carried out as previous studies (eg. [19, 20, 28]) have suggested that FIB imaging can cause grain growth in thin films, by performing counts using both techniques the extent of this growth, if any, can be estimated and accounted for in the results.

3.3 Wafer Curvature

Using a laser scanning technique [1, 9] the curvature of the films was measured at $10°C$ intervals during a temperature cycle from room temperature to 400-500$°C$ and back to room temperature. The samples were heated at $6Kmin^{-1}$ and cooled at the same rate down to $100°C$, after this point cooling of the furnace becomes sluggish and so the samples were cooled at $4Kmin^{-1}$ from $100 - 40°C$. The films were held in a protective atmosphere, maintained via a flow of nitrogen and the combustion products of a cellulose cloth in the furnace. This atmosphere was important as nickel would otherwise oxidise rapidly at elevated temperatures. The films were supported on three thermocouples, providing the temperature measure-

ment.

This apparatus has its shortfalls. The signal from the laser would, on occasion, be lost by the apparatus, this required that the oven be opened and the wafer repositioned on the thermocouples. This occurred particularly frequently during measurement below $200°C$, where this has occurred the data has been omitted. A second problem was that the strong flow of nitrogen through the chamber below $200°C$ generally led to some vibration in the samples, this is evident in the cooling data in this temperature range. For an analysis of the errors present in this method please see appendix B.

For the films on Si wafers each wafer went through at least three stress - temperature cycles, with some completing up to five. For the films on α-Al_2O_3 only one cycle was recorded for each wafer. An example cycle, showing the prominent features, is given in figure 1, such features can be used to produce graphical representations of how the film properties change with thickness as well as providing a means of comparison between cycles.

The following relations demonstrate how the gradient of any particular portion of such a cycle is directly proportional to how elastically the film is deforming:

$$\epsilon_T = \Delta T \Delta \alpha \tag{8}$$

$$M = \frac{d\sigma}{d\epsilon} \tag{9}$$

$$\frac{\Delta\sigma}{M} = \Delta T \Delta \alpha \tag{10}$$

$$\frac{\Delta\sigma}{\Delta T} = M\Delta\alpha = gradient \tag{11}$$

Where ϵ_T is the strain due to thermal mismatch, ΔT is the temperature change relevant to the calculation and $\Delta\alpha$ is the difference in thermal expansivity between

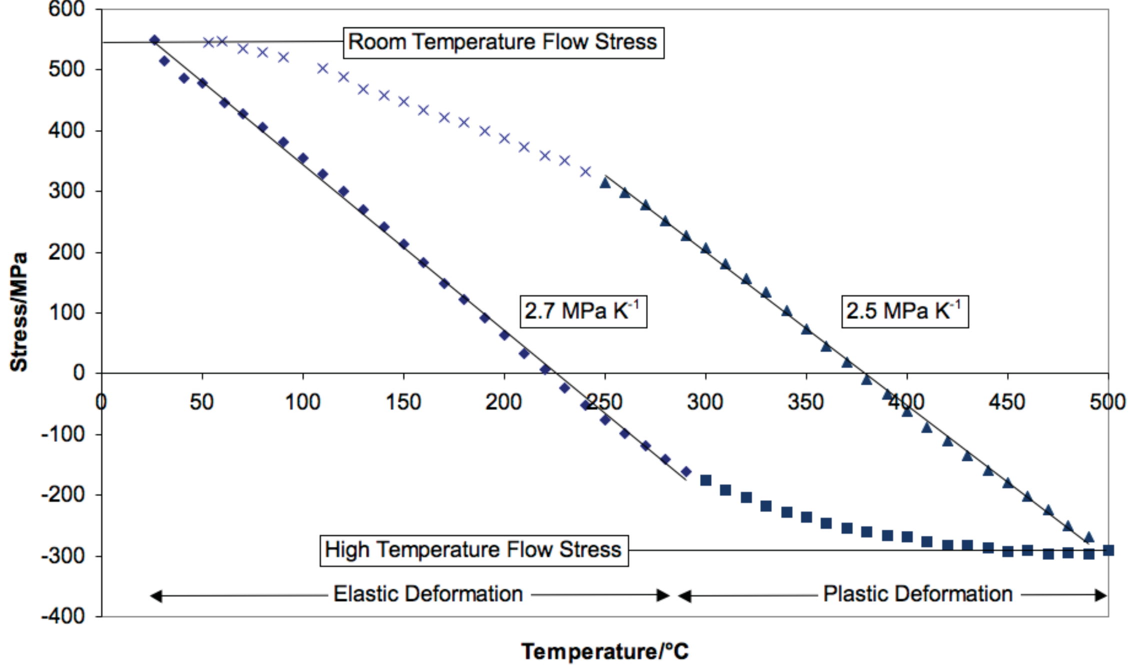

Figure 1: Stress-Temperature cycle for a 1000nm Ni film on a SiN_x/SiO_x substrate illustrating the principal points of analysis.

substrate and film. M is the biaxial elastic modulus of the film while σ and ϵ represent the stress and strain in the film respectively. Using this, an ideal elastic gradient can be calculated [2]:

For Si wafers: $\Delta\alpha = 10 \times 10^{-6}\mathrm{K}^{-1}$

$$\left(\frac{\Delta\sigma}{\Delta T}\right)_{Si} = -3.9MPaK^{-1} \tag{12}$$

For α-Al_2O_3 wafers, $\Delta\alpha = 6 \times 10^{-6}\mathrm{K}^{-1}$

$$\left(\frac{\Delta\sigma}{\Delta T}\right)_{Al2O3} = -2.9MPaK^{-1} \tag{13}$$

[2]In these relations the biaxial modulus for Ni used was $M_{(111)} = 390GPa$ and the values for α used here are $\alpha_{Ni} = 13.4 \times 10^{-6}\mathrm{K}^{-1}$, $\alpha_{Si} = 3 \times 10^{-6}\mathrm{K}^{-1}$ and $\alpha_{Al2O3}[01\bar{1}0] = 6 \times 10^{-6}\mathrm{K}^{-1}$.

To investigate the elastic deformation of the films the plan view TEM sample, as described previously, was heated *in situ*. This heating was carried out somewhat differently from the wafer curvature experiments. A TEM sample holder with a heating element was used and this holder was instructed to heat to a specified temperature. The heating rate of this set-up is rather quicker than that used for the wafer curvature apparatus and so the heating was done in a stepwise manner with target temperatures being periodically adjusted. This resulted in a typical cycle time of around 30 minutes, still significantly faster than the 70 minutes typical for a wafer curvature experiment. Because only the electron-transparent region is lacking a substrate the thermal strain over a given temperature difference is identical to that for the complete wafers. Although the reduced constraint at the interface changes the experiment slightly, only the SiN_x remains with the nickel film, it can be well approximated that the nickel film observed in this manner very closely mimics the other stress-temperature data.

4 Results

4.1 Microstructure

4.1.1 Polycrystalline Films

The results from the FIB showed that the films on Si wafers have a columnar microstructure, figure 2, and grain size analysis of images has shown that the grains have a log-normal distribution (figure 3) and a grain size approximately equal to the film thickness (figure 4). It should be noted here that the mean grain size for the 600nm film is smaller than the film thickness, folowing on from the

conclusions made by von Blanckenhagen *et al.* this smaller dimension will be used in later analyses as the confining dimension for this film.

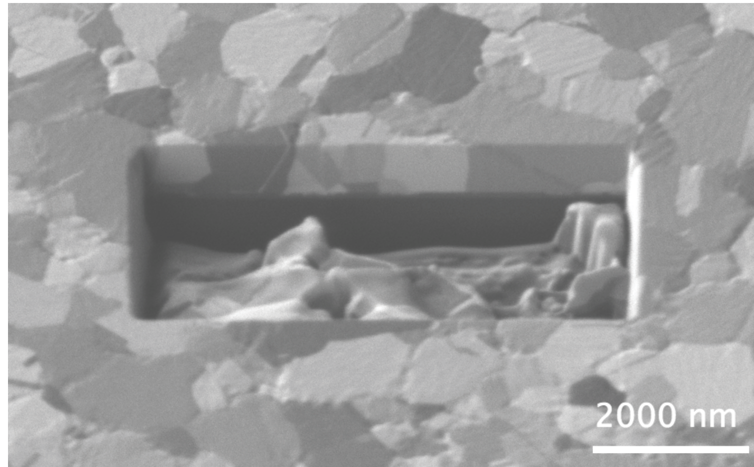

Figure 2: FIB micrograph of the polycrystalline $1000nm$ Ni film with a trench cut, the image was taken at a 45° tilt.

If a ratio is taken of the mean grain size to the film thickness it can be seen, figure 5, that this ratio is constant for the $600nm$ and $1000nm$ films but increases linearly as the films reduce in thickness below $600nm$. In addition, it should be noted that the relatively low annealing twin density, as compared to Cu, can be rationalised by comparing the stacking fault energies of some common fcc metals. Ni has a stacking fault energy of $120mJm^{-2}$ [29] compared to $55mJm^{-2}$ for Cu [**?**] and $142mJm^{-2}$ for Al [**?**], as such it is expected that fewer twins will be present than in Cu but twins are not so unfavourable that they form only rarely, as for Al.

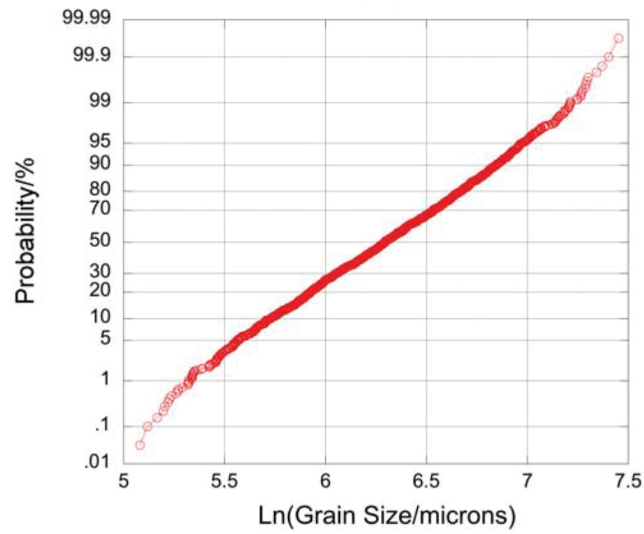

Figure 3: Probability plot for the polycrystalline 600nm Ni film, the linear data for the natural logarithm of the grain sizes confirms their lognormal distribution. Data for all the films can be found in appendix B.

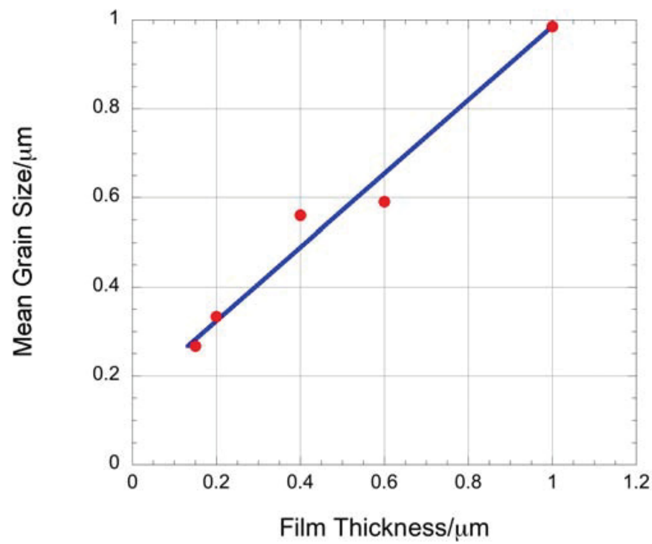

Figure 4: Plot of the film thickness against the mean grain size as determined from the FIB micrographs.

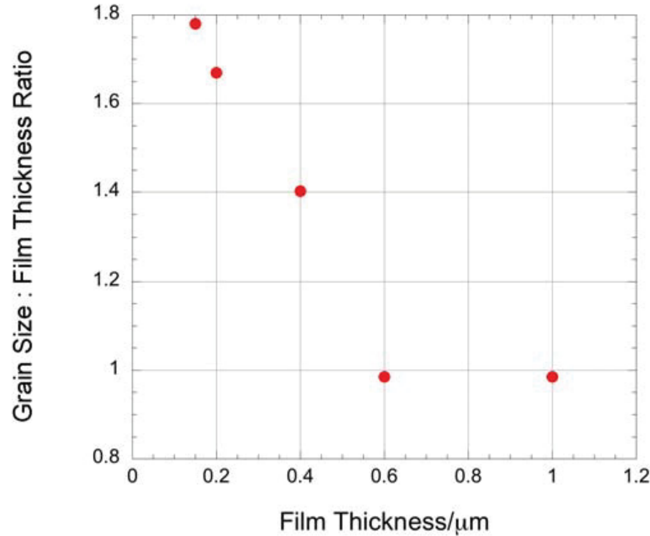

Figure 5: Plot of the film thickness against the ratio of the mean grain size, as determined from FIB micrographs, to the film thickness.

The XRD results indicate that the {111} planes are predominantly oriented parallel to the substrate with some minor deviation, as shown in figure ??. In addition it can be seen that there is no preferential orientation of the {111} planes, as evidenced by the constant intensity of the maximum at 70.5°. All the pole figures also show minor orientation maxima at 37° and 55°.

The plan view TEM sample of the 200*nm* film provided a second source of grain count statistics as well as allowing a rather higher resolution study of the microstructure. Figure 7 shows an example of the grain count images produced from the TEM.

By producing grain area counts for the 200*nm* film on SiN_x/SiO_x substrate with both FIB and TEM micrographs it was possible to produce a comparison

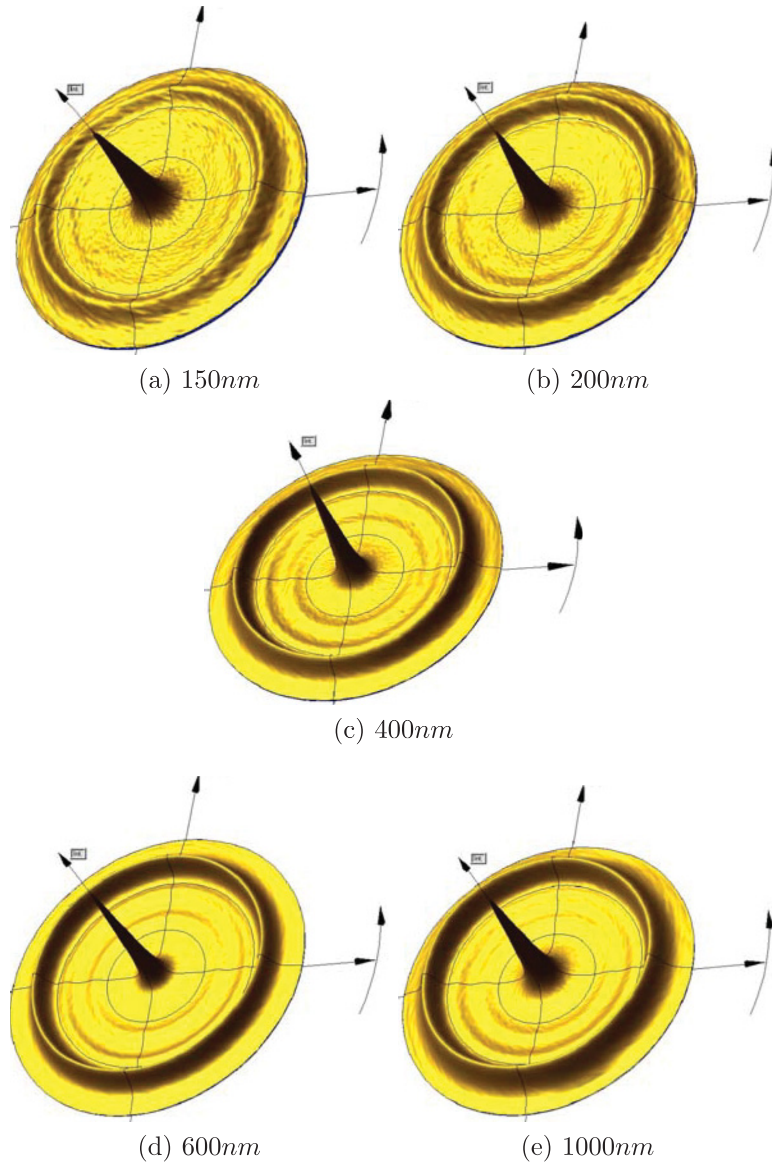

(a) 150nm (b) 200nm

(c) 400nm

(d) 600nm (e) 1000nm

Figure 6: Pole figure plots for the Ni films on SiN_x/SiO_x substrates centered on (111). ψ varies radially and φ varies tangentially in these plots.

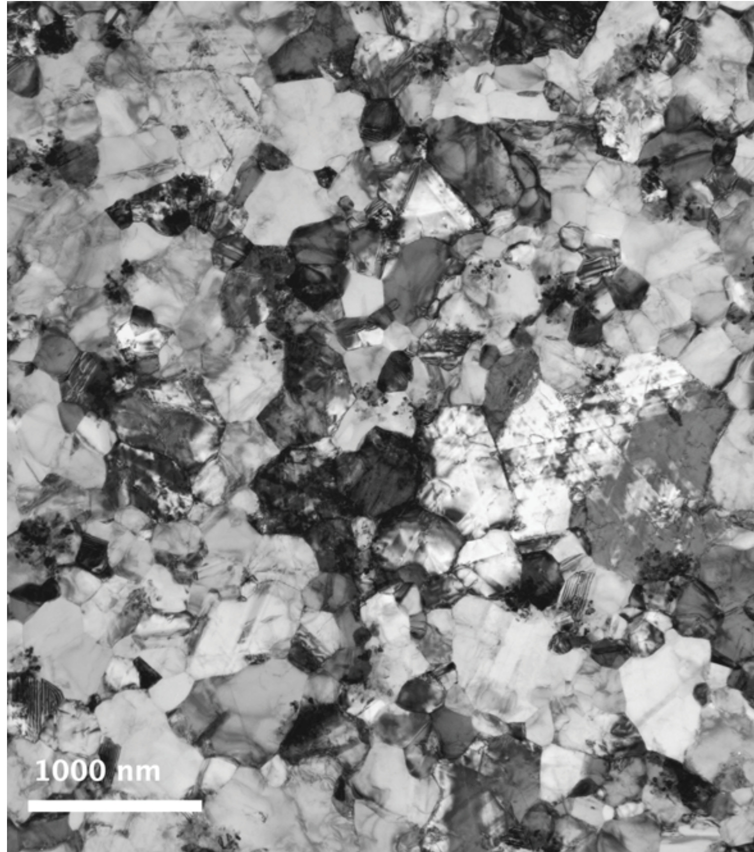

Figure 7: Bright field TEM micrograph of the $200nm$ film taken at 15kX magnification.

of these techniques. The results produced via the two techniques can be seen in figure 8. The mean grain sizes for the 200nm film as determined by FIB and TEM grain counts are 334nm and 274nm respectively.

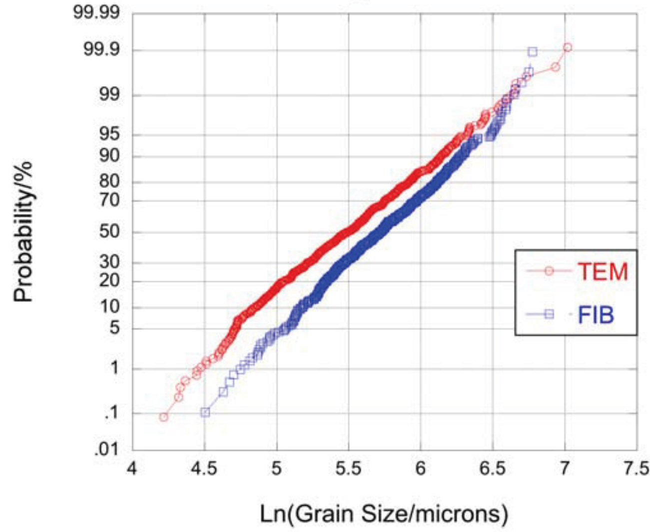

Figure 8: Probability plot for the polycrystalline 200nm film as determined from TEM and FIB data.

4.1.2 Epitaxial Films

The results from the EBSD scans confirm that the films on the (0001)-oriented α-Al_2O_3 are epitaxial although the relation between the metal and substrate was not determined in this study. Due to the films being comprised of many structural elements in one of two basic orientations an unusual grain morphology is observed, figure 9a. By utilising image quality maps and by reducing the allowable misorientation to 1° it is possible to analyse the substructure of this microstructure more clearly. Figures 9b and c show the same region as image quality plot and 1° misorientation unique grains, from this it is possible to identify the substructure making

up the 'grains' seen in figure 9. The image quality maps and 1° misorientation unique grain plots were used in tandem as complementary means of assessing the grain structure.

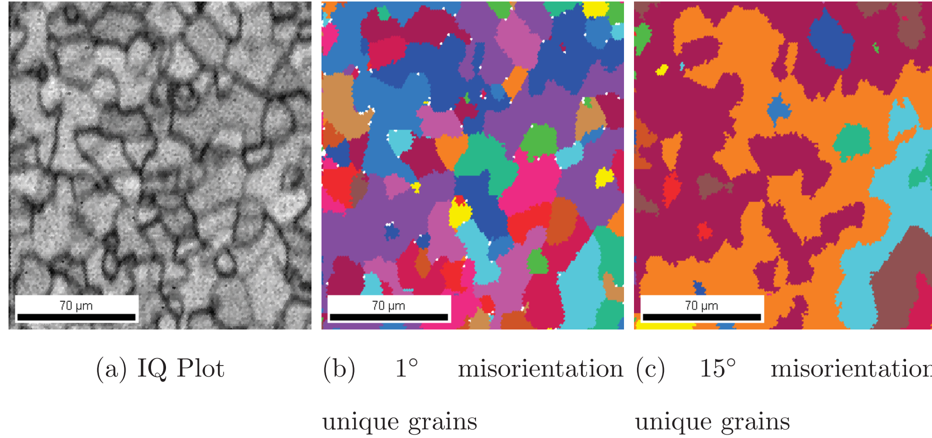

(a) IQ Plot (b) 1° misorientation unique grains (c) 15° misorientation unique grains

Figure 9: EBSD plots for the 200nm film; a) image quality map; dark areas indicate a reduction in backscatter pattern quality, b) unique grain plot with 1° misorientation limit, c) unique grain plot with 15° misorientation limit.

Using the grain statistics from the 1° misorientation settings a mean grain size was determined for each of the films, this represents an estimate for the size of the substructural elements, 10. This size is relatively stable for the 1000nm, 600nm and 400nm films but a strong deviation is observed for the 200nm film, the mean grain size is increased threefold compared to the other films.

The pole figures produced from the data provided by each scan can be seen in figure 11. This data shows two trends; the angular spread of crystallographic rotation with respect to the substrate seems to be a constant for this particular set-up (at $\sim 20°$) and the angular variation in crystallography in the direction perpendicular to the substrate increases with film thickness, figure 12.

A more complete presentation of the FIB and EBSD data can be found in

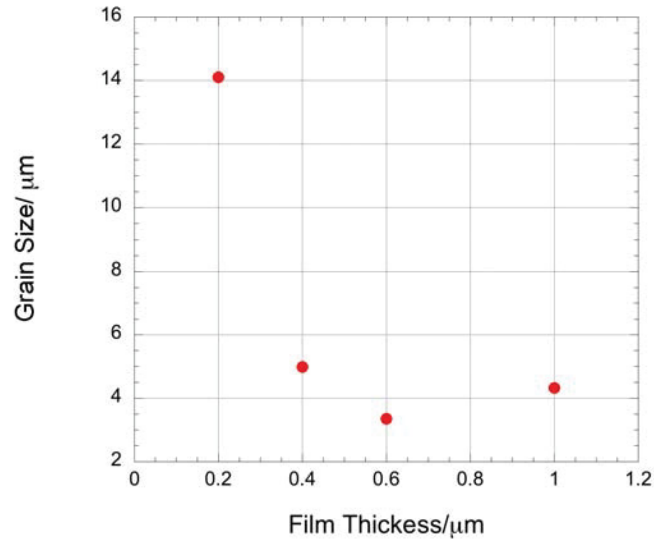

Figure 10: Plot of film thickness against mean grain size, determined from EBSD data at 1° misorientation, for the epitaxial Ni films, this represents a lower limit for the grain size.

appendix C, this includes examples of images and grain count data for all the films.

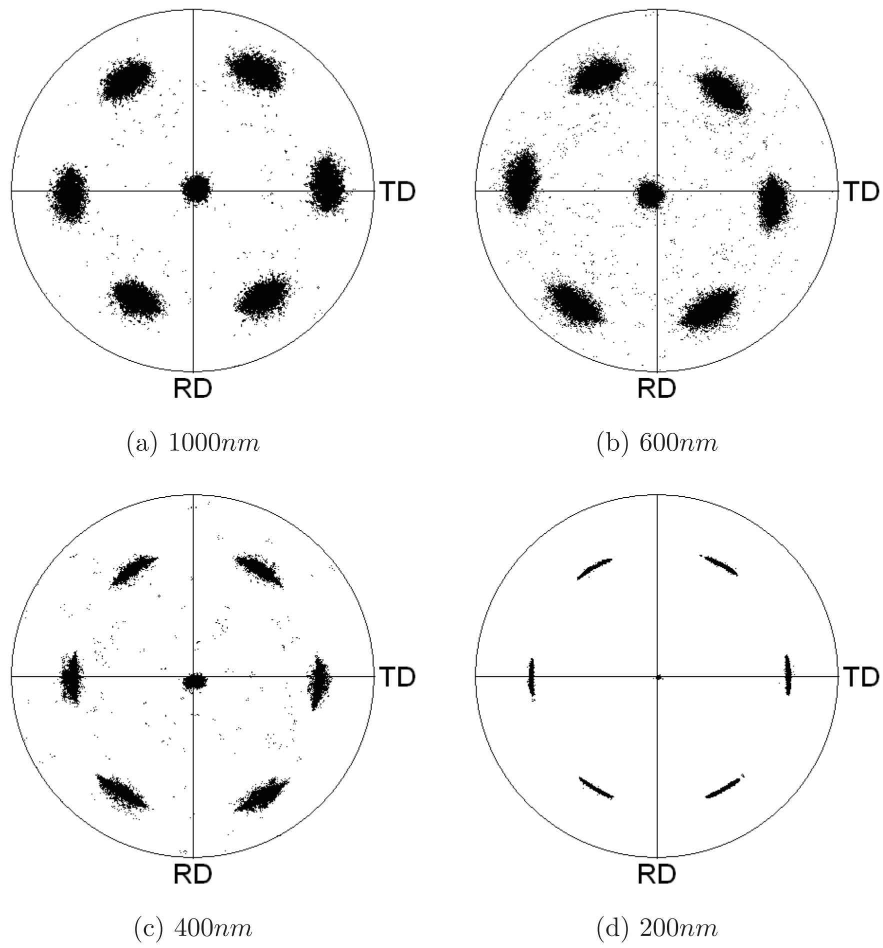

(a) 1000nm (b) 600nm

(c) 400nm (d) 200nm

Figure 11: {111} pole figures for the films on α-Al_2O_3 substrates.

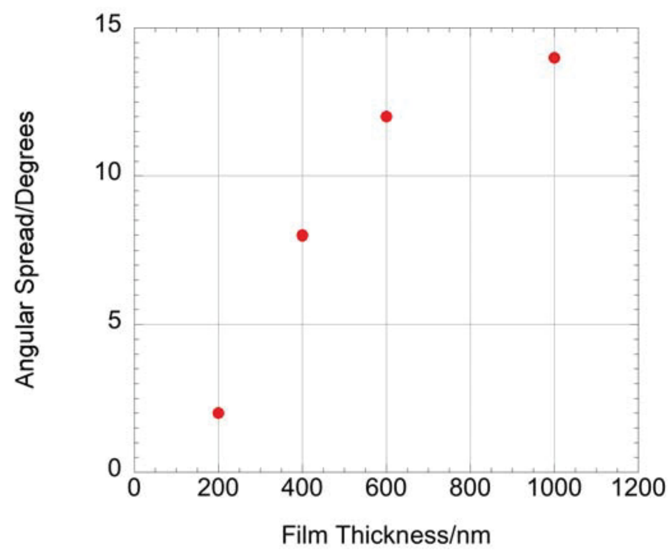

Figure 12: Plot of the angular variation in crystallography of the epitaxial films perpendicular to the substrate. Variation is determined as the angular separation, in a cross section through the centre of the data, between the 95% certainty limits.

4.2 Wafer Curvature

4.2.1 Polycrystalline Films

The data for the films on Si substrates shows several features. Firstly, figure 13 illustrates how the thermal cycling of the films produces a relatively stable series of loops with important aspects, such as the stress at room temperature, the flow stress at elevated temperatures and the slope during elastic behaviour, remaining very similar with repeated cycling.

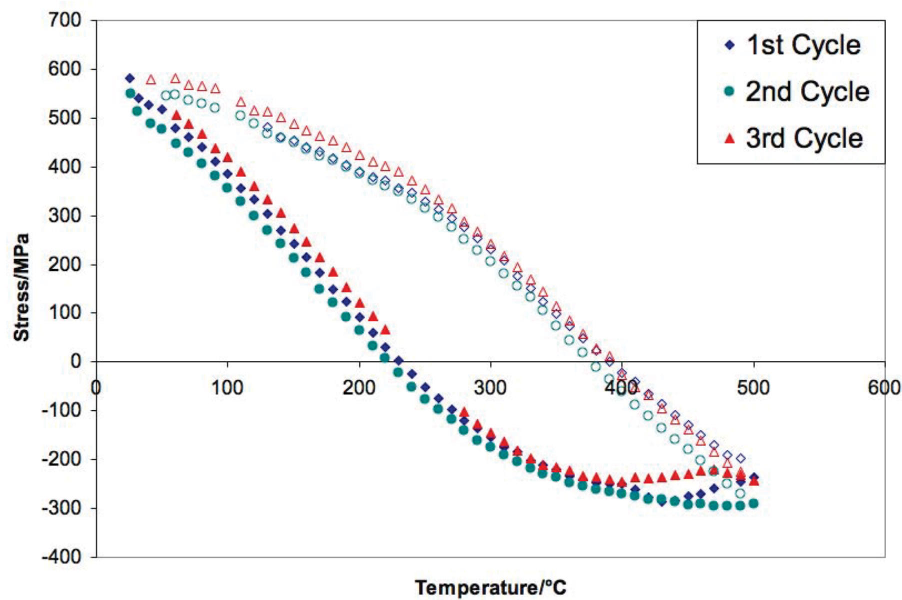

Figure 13: Stress-Temperature cycle of 1000nm Ni on SiN_x/SiO_x substrate illustrating the data stability of repeated thermal cycling.

This was not the case for two of the films, the 600nm and 150nm films. In this case the first cycles show unique behaviour while subsequent cycles are reproducible, the wafer curvature data for all the film thicknesses can be seen in appendix D. Figures 14 and 15 show the data for these two films, for both the films the first cycle demonstrated pronounced features on the heating curve. In

the case of the 600nm film the abrupt yield point in compression with no subsequent hardening is only seen in the first cycle, the gradient changes in the heating and cooling curves of the 150nm film are present during subsequent cycles but to a lesser extent.

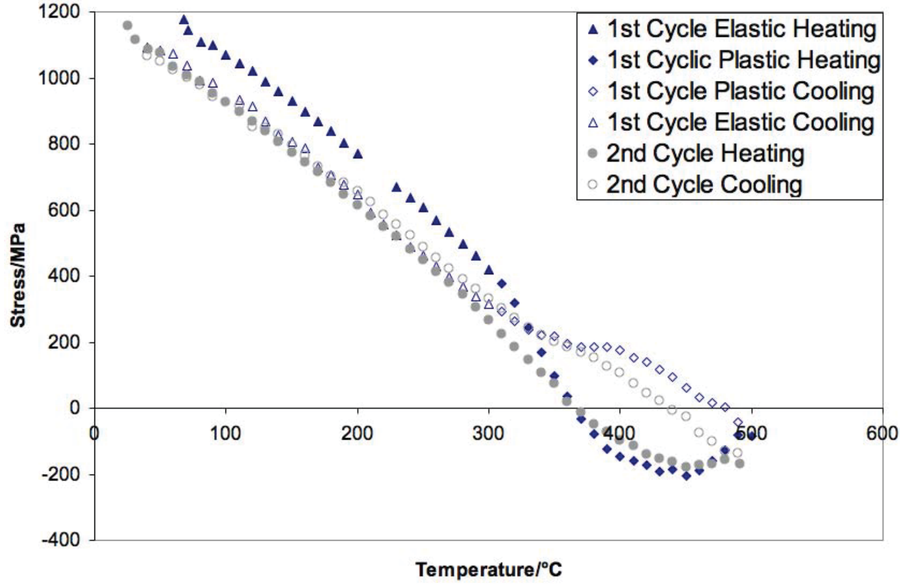

Figure 14: The initial two Stress-Temperature cycles for the 150nm Ni on SiN_x/SiO_x substrate illustrating the difference between the first and second cycles, subsequent cycles closely matched the features of the second cycle for both films.

The films thinner than 600nm all exhibit some evidence of diffusion at high temperatures, above 300°C, manifesting as gradient changes in the data. This is seen most clearly in the 150nm film, figure 14. Above 300°C the stress in the film begins to decrease with a significantly increased gradient, 7.3 versus 3.3$MPaK^{-1}$, the film then demonstrates the lowest high temperature yield of any of the films and subsequently yields at 200MPa in tension before the temperature reduces below 300°C and thermoelastic behaviour resumes. Similar, though less exaggerated, behaviour is seen in the second and third cycles and these gradient changes are

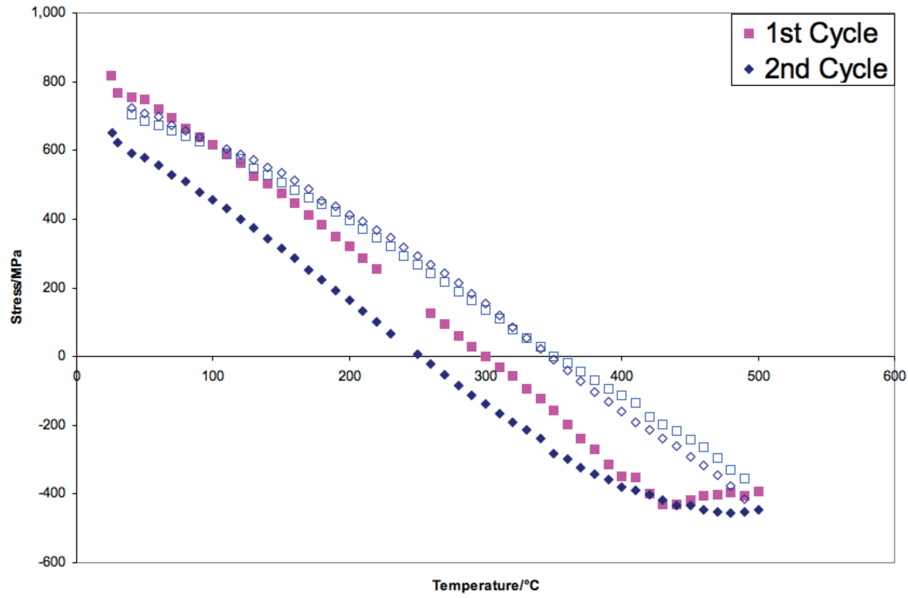

Figure 15: The initial two Stress-Temperature cycles for the 600nm Ni on SiN_x/SiO_x substrate illustrating the sharp yield and steady flow in the first cycle, subsequent cycles closely matched the features of the second cycle for both films.

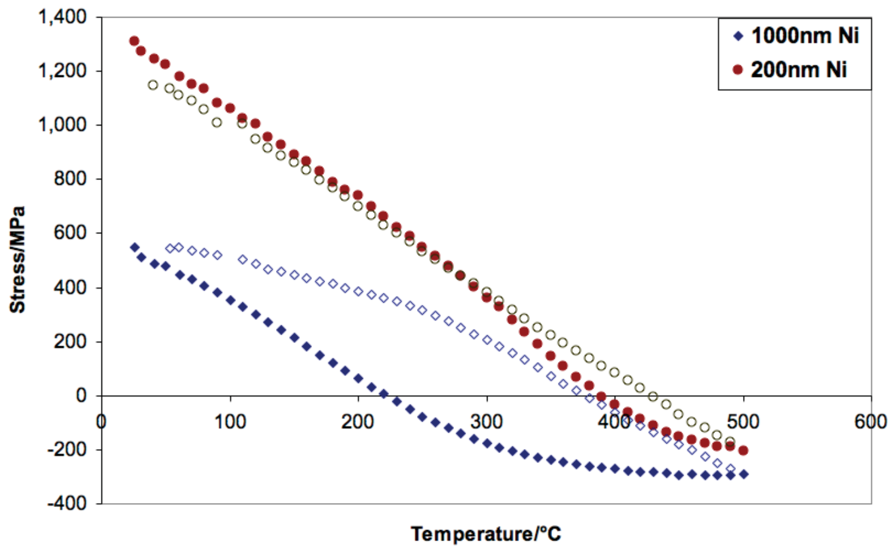

Figure 16: Stress-Temperature cycles for the 200nm and 1000nm Ni films on SiN_x/SiO_x substrate showing the strong dependence of the film properties on thickness.

also observed in the $200nm$ and $400nm$ films.

Another prominent feature is the strong difference between the film thicknesses, figure 16. A quick means of quantifying this difference is to compare the elastic and plastic strain, as defined in figure 1, for each of the film thicknesses, table 1.

Film Thickness / nm	**Substrate**	$\epsilon_{\mathbf{el}}$ / %	$\epsilon_{\mathbf{pl}}$ / %
1000	SiN_x/SiO_x	0.20	0.28
600	SiN_x/SiO_x	0.28	0.20
400	SiN_x/SiO_x	0.43	0.06
200	SiN_x/SiO_x	0.45	0.04
150	SiN_x/SiO_x	0.32	0.17
1000	α-Al_2O_3	0.13	0.22
600	α-Al_2O_3	0.24	0.11
400	α-Al_2O_3	0.27	0.08
200	α-Al_2O_3	0.36	0

Table 1: A summary of the mean elastic and plastic strains experienced by the films.

By plotting the yield stresses for the different thicknesses against inverse film thickness it is possible to obtain a linear plot if the films are deforming via dislocations on inclined planes, as suggested by Nix [1]. Figure 17 shows such a plot of inverse film thickness against the room temperature yield stress. Linearity appears to only be present for the films greater than $400nm$ in thickness. For the films thinner than $400nm$ a plateau of around $1100MPa$ is reached for the room temperature yield. There is approximately a factor of two difference in the room temperature stresses observed for these films.

The high temperature yield data is rather more complicated, with the value varying by the same factor of two but with a maximum for the $600nm$ film and a minimum observed for the $150nm$ film, figure 18.

In order to investigate the features observed in the cycles in some more depth

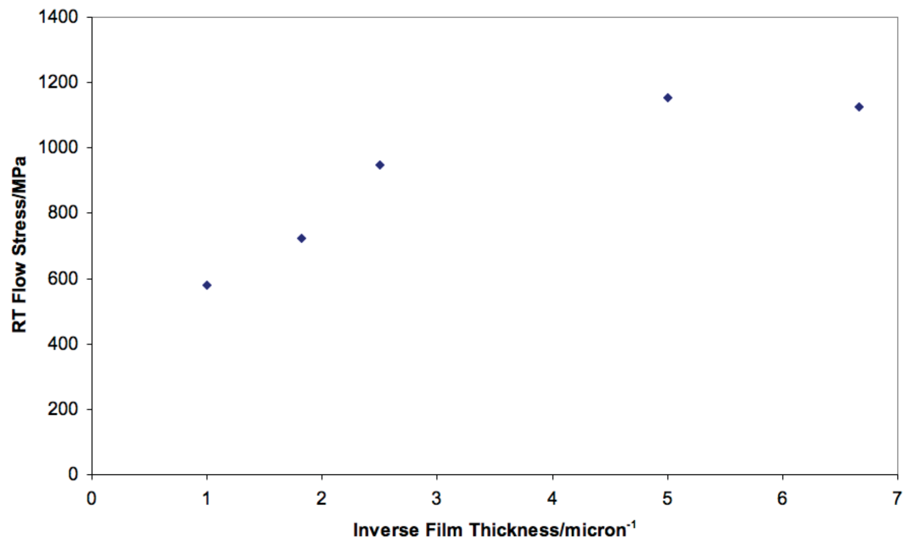

Figure 17: A plot of the stress recorded in the films on SiN_x/SiO_x substrates at room temperature at the end of the thermal cycles against the inverse film thickness.

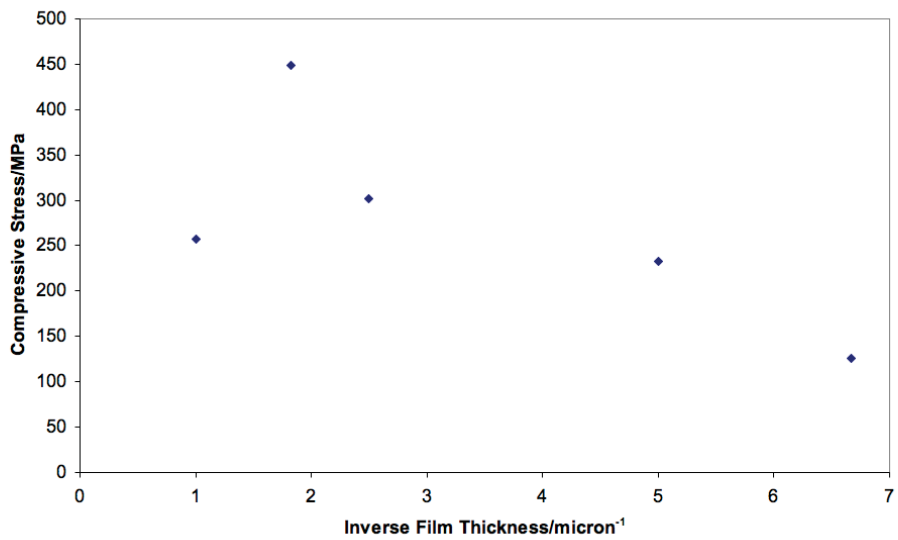

Figure 18: A plot of the compressive stress recorded in the films on SiN_x/SiO_x substrates at 500° against the inverse film thickness.

the 600nm film was cycled to three different maximum temperatures, figure 19. The first point of note is that the room temperature yield increases with increasing maximum temperature, and hence strain. The second point is that even the cycle to 400°C shows appreciable hysteresis, despite this temperature being chosen as the film seemed to be behaving thermoelastically up to this point in earlier cycles. The cycle with a temperature maximum of 550°C closely matches the 500°C cycle but exhibiting stresses 50-100MPa higher during cooling, due to the extra strain.

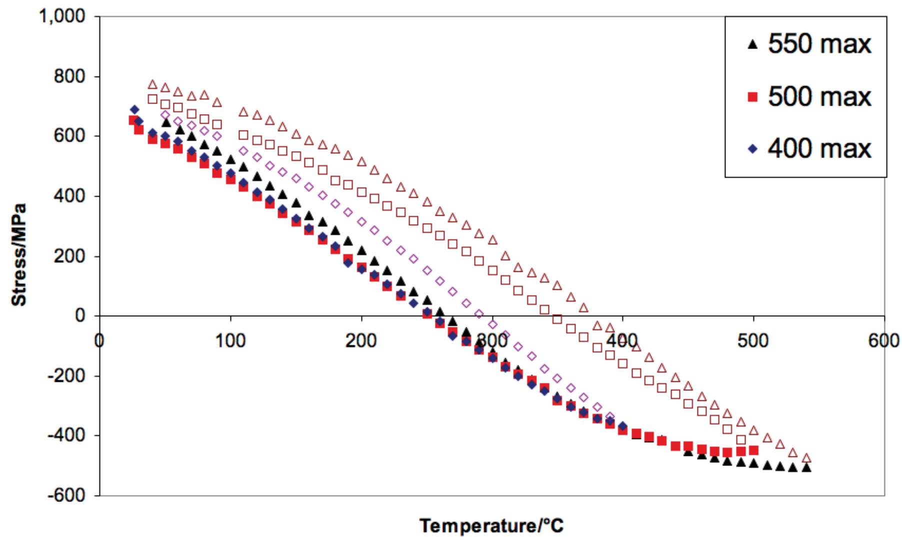

Figure 19: Stress-Temperature cycles for the 600 nm Ni film on SiN_x/SiO_x substrate with the maximum temperature of the cycle varied from 400 to 550°C.

The *in situ* stress-temperture testing also yielded some interesting results. This experiment could only be performed with the 200nm film due to limitations on electron transparency in TEM. Figure 20 shows a series of images captured in the 400-500-400°C range of the cycle. Figure 20a shows the initial arrangement of dislocations in a grain, with 6, those highlighted, on two parallel planes in the top corner of the grain. Figures 20b-d illustrate the gradual glide of 4 of these dislocations across the grain. Figure 20e shows the dislocations in their final

positions at the other side of the grain as the maximum temperature is reached, note that the dislocations stay in the grain rather than being absorbed by the grain boundary. Figures 20f-h illustrate the subsequent return of the dislocations as the cooling cycle begins. By comparing figures 20a and 20h we can see how the process of dislocation glide is, in this case, quite reversible; the slip traces on the glide planes are the only real difference between the two images. By calculating the strain due to the glide of 5 dislocations across the grain it was found to be $\sim 0.1\%$ for this grain, 2.5x that observed globally for this 200nm film.

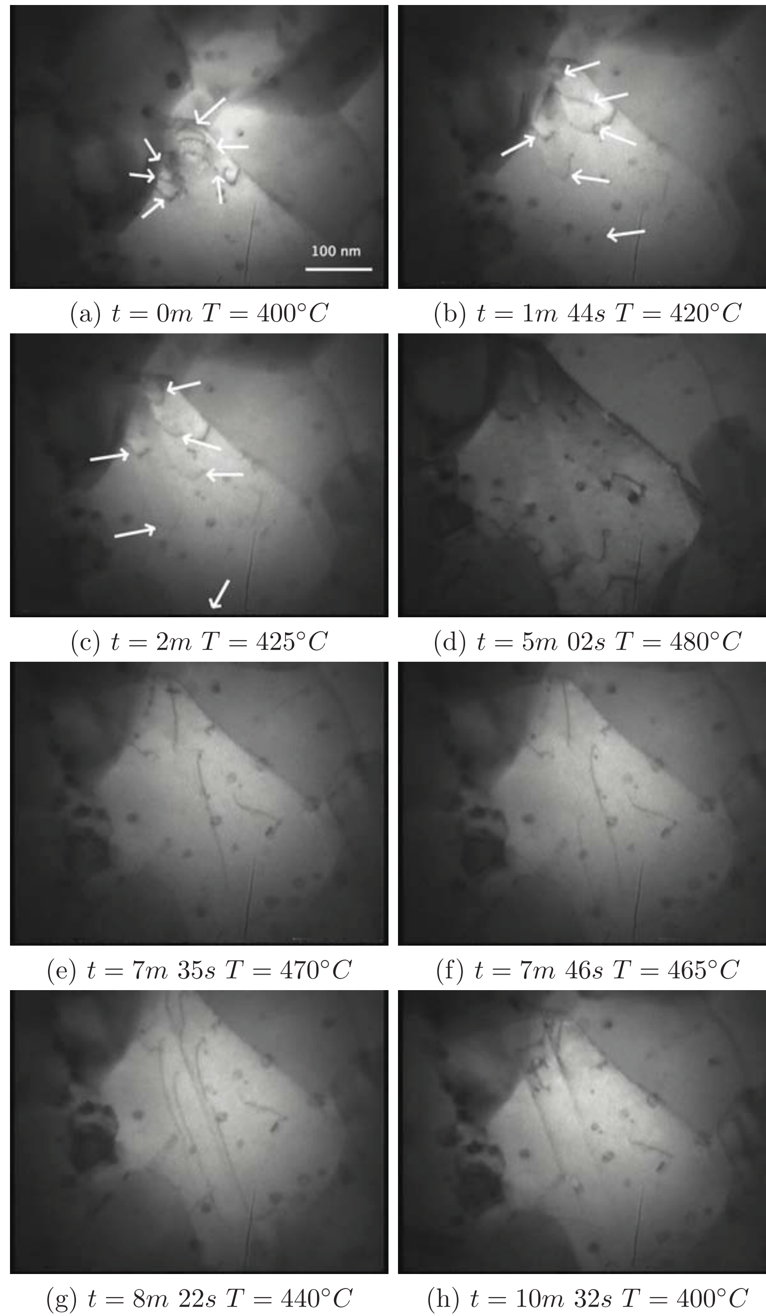

(a) $t = 0m\ T = 400°C$ (b) $t = 1m\ 44s\ T = 420°C$

(c) $t = 2m\ T = 425°C$ (d) $t = 5m\ 02s\ T = 480°C$

(e) $t = 7m\ 35s\ T = 470°C$ (f) $t = 7m\ 46s\ T = 465°C$

(g) $t = 8m\ 22s\ T = 440°C$ (h) $t = 10m\ 32s\ T = 400°C$

Figure 20: Stills from an *in situ* TEM experiment on the $200nm$ film on SiN_x/SiO_x.

4.2.2 Epitaxial Films

The first point to note when examining the data for the films on α-Al_2O_3 is the increased scatter of the data. This is an unavoidable consequence due to the increase in substrate thickness and stiffness compared to the Si wafers. A comparison of the errors in stress measurement can be found in appendix C.

The films on α-Al_2O_3 also show a general increase in yield strength with reducing film thickness, this is illustrated in figures 21 and 22.

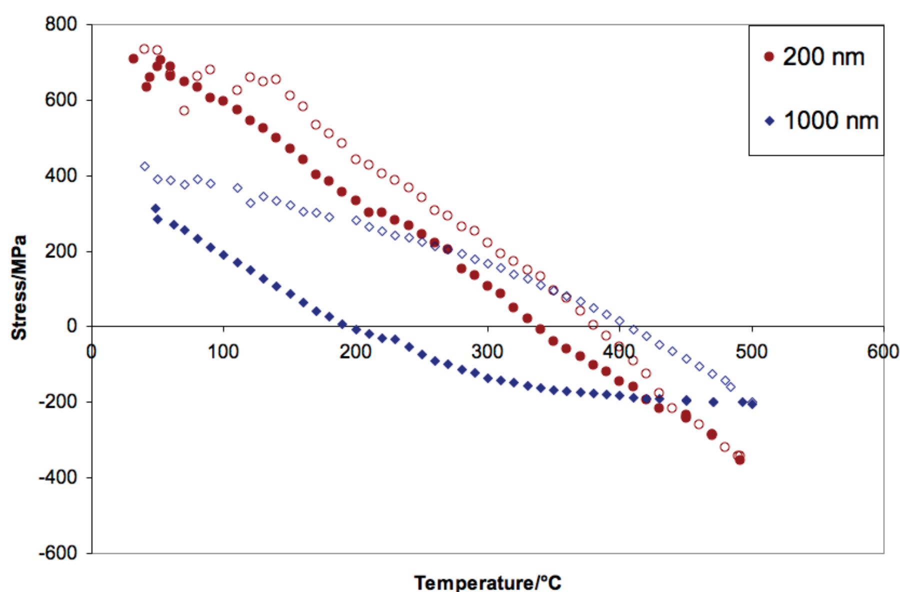

Figure 21: Stress-Temperature cycles for the 200nm and 1000nm Ni films on α-Al_2O_3 substrate showing a similar dependence of properties on film thickness but with lower absolute stresses recorded.

This reduction in yield stress is also seen very clearly in the high temperature yield stress for these films, figure 23. The data at high temperatures had both a reduced slope and reduced intercept compared to the data at room temperature.

The 200nm cycle data shows one peculiar feature. The film data shows a constant modulus on heating but initially demonstrates an elevated value as cooling

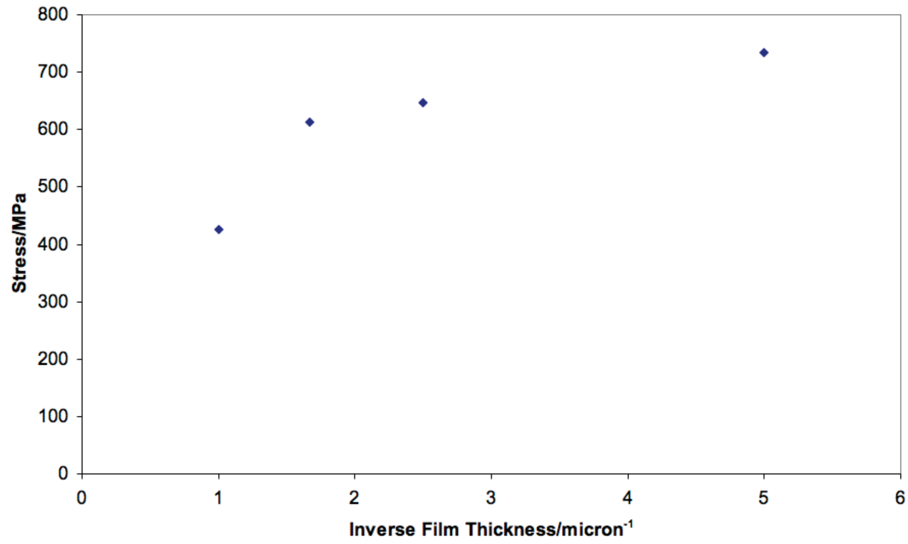

Figure 22: A plot of the stress recorded in the films on α-Al_2O_3 substrates at room temperature at the end of the thermal cycles against the inverse film thickness.

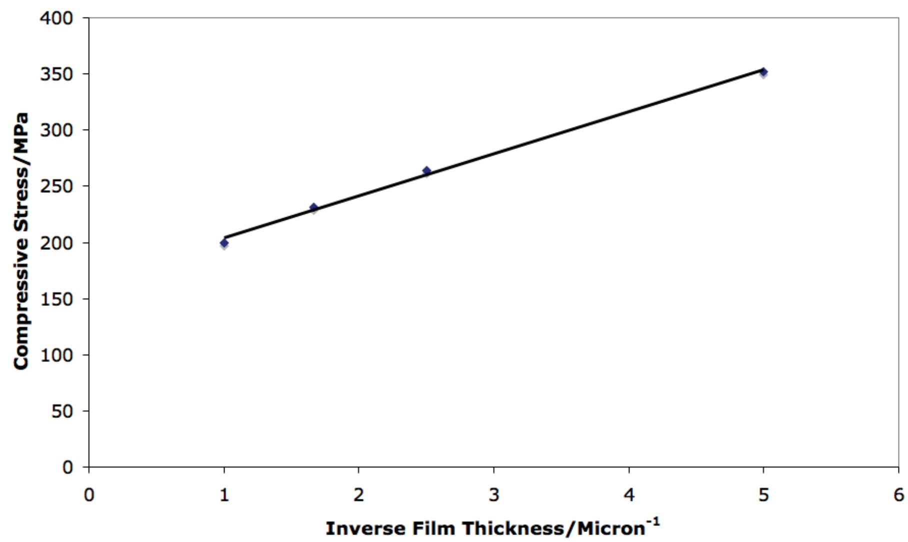

Figure 23: A plot of the compressive stress recorded in the films on α-Al_2O_3 substrates at 500° against the inverse film thickness. The slope is $37.4 MPa\mu m$ and the intercept is $167 MPa$.

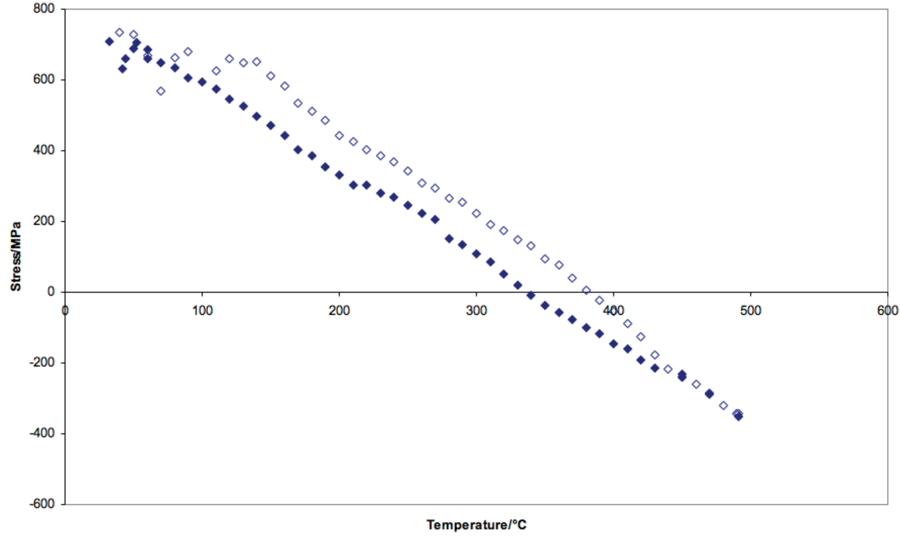

Figure 24: Stress-Temperature cycle for the 200nm Ni film on an α-Al_2O_3 substrate, scatter in the low temperature cooling data is an experimental artefact.

begins, figure 24. At about 100MPa tension the modulus returns to the value observed on heating before scatter in the signal obscured any further analysis.

4.2.3 Thermomechanical Gradients

A feature demonstrated by the films on both substrates is the variation in the 'elastic' modulus with film thickness, figures 25 and 26. For the films on Si wafers there are two noteworthy features. Firstly, the difference between the 'elastic' slope on heating and cooling seems to reduce with the film thickness, the 1000nm film shows an 8% reduction in slope from heating to cooling and the 600nm 2% reduction while the three other films demonstrated less than 1% deviation. Secondly, an overall trend for 'elastic' slope to increase as the film gets thinner is present, this is also observed for the films on α-Al_2O_3 and in both cases this trend is linear. It should also be noted that the data for the 150nm film on Si does not fit this trend. The increased scatter in the data for the films on α-Al_2O_3 is due to the

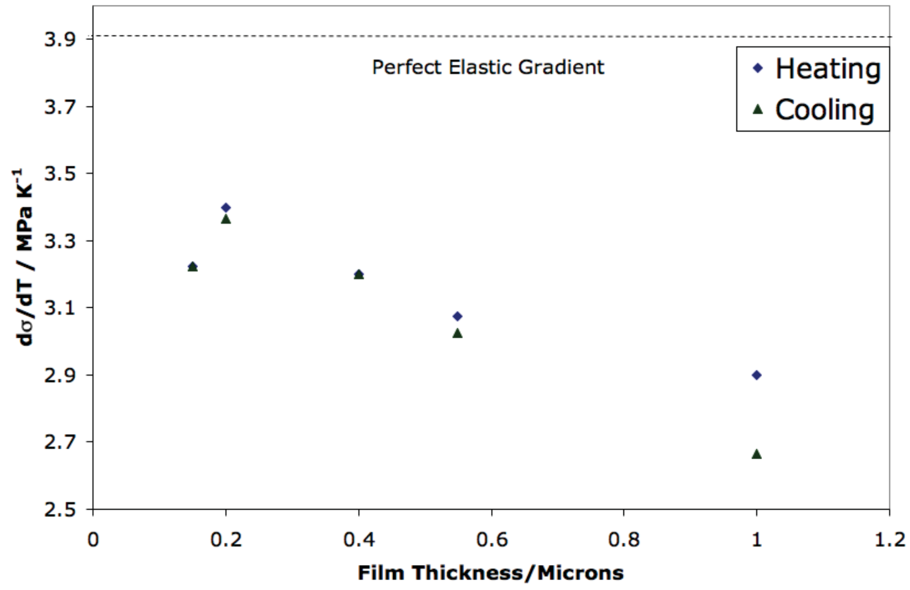

Figure 25: A plot of the thermoelastic slopes observed during heating and cooling of Ni films on a SiN_x/SiO_x substrate. The dashed line indicates the ideal slope expected due to thermal mismatch between the materials.

enhanced error when working with the stiffer α-Al_2O_3 wafers and the reduction in the amount of data.

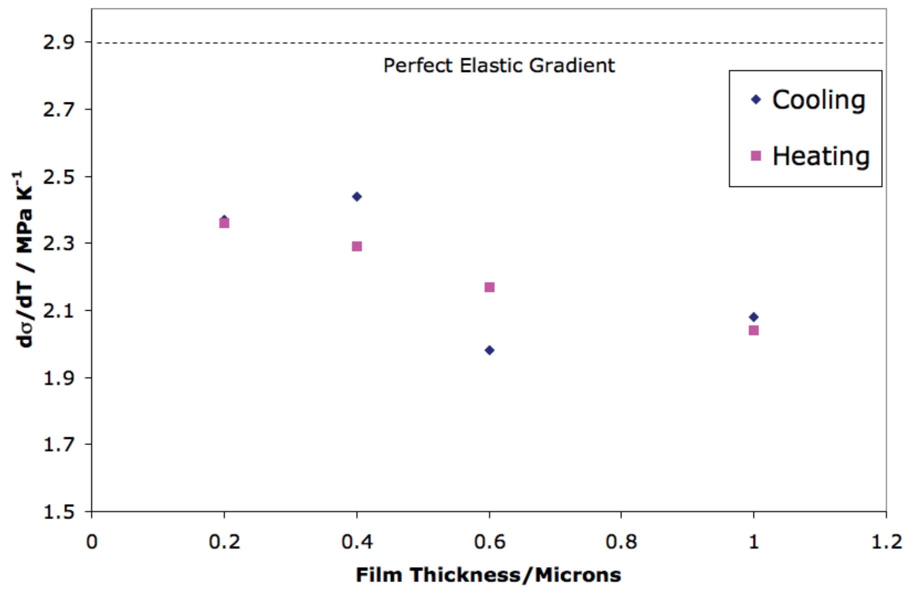

Figure 26: A plot of the thermoelastic slopes observed during heating and cooling of Ni films on an α-Al_2O_3 substrate. The dashed line indicates the ideal slope expected due to thermal mismatch between the materials.

5 Discussion

5.1 Microstructure

The pole figure, TEM and FIB data all confirm that the polycrystalline films on SiN_x/SiO_x substrates have a very strong {111} texture parallel to the substrate with columnar grains demonstrating a lognormal distribution. This is the same result as has been found for Al [3], Cu [4] and NiAl [5] for films in this thickness range. The grain size, 1 - 1.5 times the film thickness, is also equivalent to what has been previously found for films deposited in these conditions.

The smaller peaks in the pole figure data at 37° and 55° respectively can be attributed to {100} and {110} type planes lying parallel to the substrate as minor texture components.

The statistical evidence from the grain counts made of the $200nm$ film suggests that a degree of grain growth is occurring during FIB imaging. This effect will be most pronounced in the thinner films where the surface area to volume ratio is greatest. In addition, the volume of material required to diffuse such that a given increase in grain area is achieved reduces with film thickness. As such I would suggest that this is a contributing factor to the apparent increase in grain-size to film thickness ratio as the film thickness is decreased. However, the TEM data produces a mean grain size to film thickness ratio of 1.4 compared to 1.6 for the FIB data, this remains large compared to the ratio of $\sim$1 observed for the $600nm$ and $1000nm$ films. This suggests that the increased ratio of the mean grain size to film thickness for the thinner films is a real effect and not purely an artefact of the imaging process.

The pole figure data for the epitaxial films indicates that a strong epitaxy

is present, with the two twin-related crystallographic alignments producing the 6 maxima at 70.5° from (111). The constant rotational spread of this alignment with respect to the substrate indicates that the thermodynamic stability of the epitaxy with respect to rotation is invariant in this thickness range. In contrast, the angular variation in the crystallography perpendicular to the substrate shows significant variation with film thickness. The angular variation increases linearly with film thickness initially but then begins to plateau for the 1000nm film, with only four thicknesses, one film for each, it is not possible to comment on the certainty in this trend. It can however be noted that the angular variation observed for the 1000nm epitaxial film is very close to that observed for the polycrystalline films on an amorphous substrate while the variation observed for the 200nm film is far smaller than this.

The 1° misorientation EBSD data provides a lower limit to the grain size, of any of the epitaxial films, at around 4 μm. With the grain misorientation set to 15°, such that low angle boundaries between grains are not included, the size of the grains is significantly larger still. As such the effect of the grain boundaries in the material has clearly been reduced, although not entirely eliminated. Peculiarly, the 200nm epitaxial film exhibits a particularly coarse grain structure. As no trend is clear from the grain sizes of the other epitaxial films it is suggested here that this coarse grain structure is a result of unknown differences in the substrate or deposition conditions for this particular film.

5.2 Wafer Curvature

It has been reported several times [3, 5, 31] that the first stress-temperature cycle in this type of experiment is quite different to subsequent, highly reproducible cycles. This can occur for several reasons. These include; microstructural instability, the formation of passive oxide layer [5] and a low starting strain due to stress relaxation in the film [31]. In the case of these nickel films the 15 min at $600°C$ anneal following sputtering should have stabilized the microstructure and ensured an initial stress in the film similar to what would be achieved during the cycles to be performed. Two of the films did however demonstrate a difference between the first and subsequent cycles, the $150nm$ and $600nm$ films.

In the case of the $150nm$ film the first cycle shows the strong influence of diffusion at temperatures above $300°C$, this effect is less pronounced in subsequent cycles. A possible explanation for this is that a thin oxide film forms on the surface of the film during the first cycle, this film then interferes with the diffusive processes in subsequent cycles.

For the $600nm$ film the first cycle shows an abrupt yield on the first cycle not observed in subsequent cycles. The yield during heating in the first cycle occurs at over $400MPa$ while during further cycling deviation from thermoelastic behaviour occurs at 200-300 MPa. The return thermoelastic slope also has an unusually low slope, $2.5MPaK^{-1}$, compared to that observed for subsequent cycles, 3 - 3.5 $MPaK^{-1}$. It is possible that the difference observed here is due to dislocation nucleation. If the $600nm$ film happened to be particularly dislocation free then it would require a large stress to nucleate the dislocations necessary for the film to yield in compression. Once the critical point was reached however the film would

be able to yield freely at that stress, the dislocations nucleated in this process may also be responsible for the reduced thermoelastic slope on cooling as local deformation due to stress variations in the film would reduce the rate at which stress increased.

The trend observed in the room temperature yield stresses of the polycrystalline films, linearity for the inverse thickness for thick films with a plateau, has been observed by several other authors [3, 4, 5]. Figure 27 shows a chart of the data for Al, Cu and Ni plotted together, the values have been normalised by the shear modulus of the metal. The data for the three fcc metals clearly follow one trend. The work of Eiper *et al* [25] suggests that the plateau observed is not a result of a change in deformation mechanism but is rather due to the films not being subjected to a sufficient strain to cause yield at room temperature. This conclusion is supported by the data presented here for a $600nm$ film subjected to varying strain, the room temperature yield point increasing with the strain in the film.

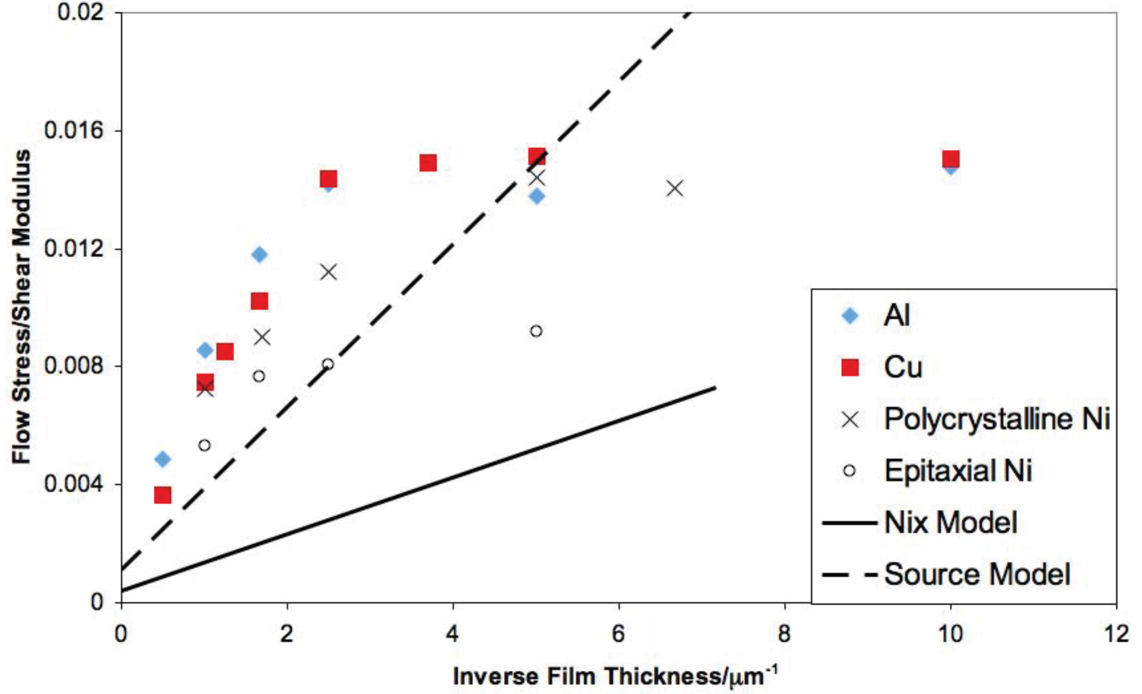

Figure 27: A plot of room temperature yield data for Cu, Al and Ni, normalised by their respective shear moduli ($42GPa$ for Cu, $25GPa$ for Al and $80GPa$ for Ni), versus the inverse film thickness. The line illustrates the prediction of the Nix model made using the following parameters: $\varphi = 70.5°$, $\lambda = 35.3°$, $b = 0.249nm$, the shear modulus of α-$Al_2O_3 = 185GPa$ and $\beta_s = 2$.

The data for the films on α-Al_2O_3 shows some agreement in the dependence of the film thickness with stress to the Nix-Freund model [1, 11], this model predicts a slope of $64MPa\ \mu m$ for films on an α-Al_2O_3 substrate; a slope of $63.8MPa\ \mu m$ was observed in this study. The data does however show a raised intercept with the stress axis and this is not accounted for in the present theory, the physical significance of this is unclear. In addition to this it is not clear if the $200nm$ film truly yields and hence should be included when calculating a trendline. Table 2

gives a comparison of the stresses measured in the Ni films at room temperature with those predicted by the Nix–Freund model and von Blanckenhagen's dislocation source model. The values predicted by the Nix–Freund model for the films on α-Al_2O_3 are consistently $\sim 300MPa$ smaller than those measured while von Blanckenhagen's model underestimates the stresses for the thicker polycrystalline films but overestimates once the plateau in stress is reached.

Film Thickness/nm	$\sigma_{\mathbf{RT}}$ **(poly)**	$\sigma_{\mathbf{RT}}$ **(epi)**	$\sigma_{\mathbf{Nix}}$ **(Si/**α**-**$\mathbf{Al_2O_3}$**)**	$\sigma_{\mathbf{vB}}$
1000	579	425	74/103	320
600	723	613	120/160	570
400	948	646	170/230	780
200	1153	734	300/420	1570
150	1125	–	390/540	2090

Table 2: Numerical comparison of experimentally determined room temperature stresses and those predicted by theory. All stresses are in MPa. For σ_{vB} s_{eff} was taken to be $h_f/4$.

In the films on both substrates a trend was observed between the film thickness and the thermoelastic slope. In both cases the slope increased in a linear fashion with decreasing film thickness, this phenomenon was also observed by Wellner [26] for NiAl films deforming plastically. Wellner also observed a change in the slope of the thermoelastic curve on cooling from different maximum strains. This can also be seen to some extent in the data presented here for the $600nm$ film subjected to different maximum strains; the slope on cooling for the lower $400°C$ maximum was $3.5MPaK^{-1}$ compared to the $2.5 - 3.1MPaK^{-1}$ observed for the other cycles

where straining was greater. The work presented here also suggests that different processes are at work in the heating and cooling thermoelastic slopes, particularly in the 600nm and 1000nm films. These results all indicate that local plastic deformation is occurring during this apparently elastic regime, hence also why the slope of these thermoelastic regions is always less than that of the calculated slope due to thermal mismatch between film and substrate.

This work strongly suggests that dislocation glide is occurring in a stable manner within larger grains during this thermoelastic regime. As a very strong fibre texture is observed for these films and the films are subjected to a biaxial stress it is expected that grain size is the determining factor in which grains exhibit plastic deformation. Further support for local plastic deformation was found during the *in situ* tests. Figure 28 shows a grain in the 200nm film, this grain was observed during two temperature cycles to $500°C$ and back to room temperature. At a grain diameter of around 1000nm it is one of the larger grains observed in this film. In the imaging conditions used several dislocations were observed gliding in the grain during heating and cooling, this was despite the stress-temperature cycle for this film suggesting that little, if any, dislocation activity was present.

Constrained diffusional creep has been suggested as an important plastic deformation mechanism in films such as these by Gao et al [12] and modelling by Weiss et al. [13] has shown that Gao's creep model can explain some features of the curves. As with all diffusional-controlled plasticity constrained diffusional creep operates most efficiently for thinner films with smaller grain sizes and at higher temperatures as this ensures shorter diffusion paths and higher atomic mobility respectively.

The plot of the high temperature flow stress of the films on Si wafers shows a

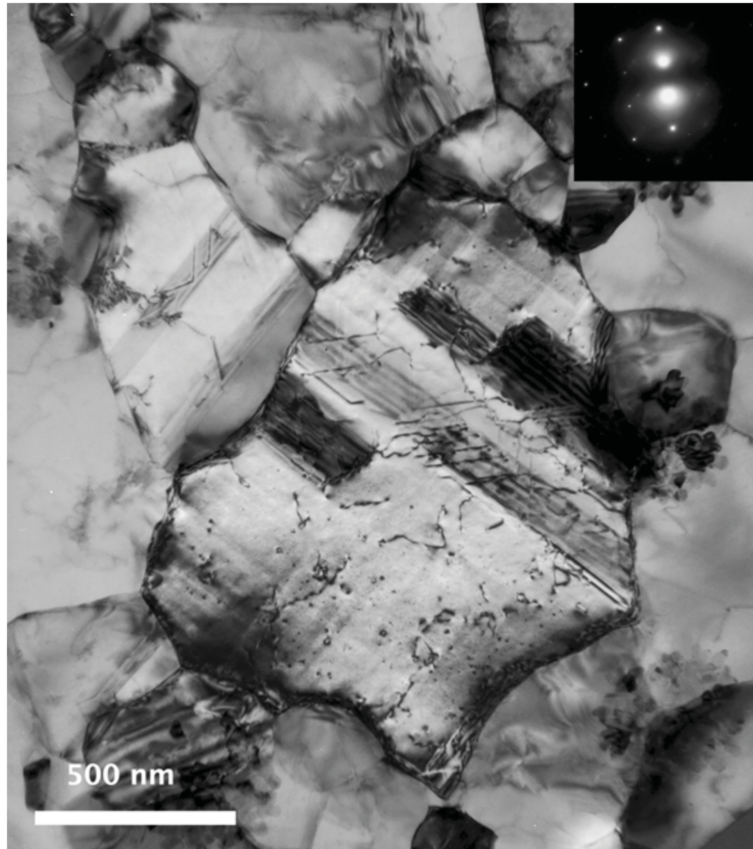

Figure 28: TEM image of a grain in a 200nm Ni film on a SiN_x/SiO_x substrate.

double trend. In addition to this the cycles for the films thinner than 600nm suggest some diffusion controlled plasticity, evidenced by changes in slope at elevated temperatures. As such it is put forward here that the double trend observed in this data is due to the competing mechanisms of dislocation plasticity and constrained diffusional creep. The data for the films on α-Al_2O_3 however show a linear trend for inverse film thickness but with a greatly reduced slope. This supports the conclusion that the diffusion observed is grain boundary mediated, the lower energy boundaries and larger grains in the films on α-Al_2O_3 prevents constrained diffusional creep from becoming dominant.

6 Summary

The investigation of the film microstructure found that the polycrystalline films on SiN_x/SiO_x substrates had a columnar microstructure in which a strong texture of {111} parallel to the substrate was present. A comparison in grain count statistics was made between FIB and TEM micrographs, this suggests a degree of grain growth during FIB imaging. In general the mean grain size of the polycrystalline films scaled linearly with the film thickness and the ratio of mean grain size to film thickness increased with decreasing film thickness but this increased ratio cannot be wholly attributed to ion-beam induced grain growth.

The films deposited onto α-Al_2O_3 demonstrate two broad, twin-related, crystallographic alignments with respect to the substrate, the degree to which the crystallography is aligned perpendicular to the substrate varies with film thickness. Due to the two possible alignments an unusual microstructure develops, although it is possible to estimate the 'grain' size by setting the allowable misorientation with a grain to a very low value, in all cases this produces a mean grain size significantly in excess of the film thickness.

The investigation of the thermomechanical properties of the polycrystalline films has highlighted several trends. The yield stress at room temperature increases with the inverse of film thickness until a plateau is reached, the plateau is produced due to these thinner films exhibiting higher yield stresses that could not be thermally strained sufficiently to induce yield. Additionally it was found that the gradient of the thermoelastic slope increased with decreasing film thickness

and discrepancy between the thermoelastic slope in heating and cooling was found to decrease with decreasing film thickness. This effect is due to local dislocation plasticity operating during this apparently elastic regime, the smaller grain sizes in the thinner films inhibits this.

The high temperature yield data for the polycrystalline films showed a dual trend, with the 600nm film exhibiting the highest yield stress in this compressive regime. This was determined to be due to a competition between dislocation controlled plasticity and diffusion controlled plasticity, the 150nm film in particular showed stress relaxation in excess of that due to thermal mismatch at elevated temperatures.

The epitaxial films demonstrated an inverse film thickness dependence of the yield stress at both room temperature and at elevated temperature. The data for the yield stress at room temperature shows some agreement with the Nix-Freund model. As such this has shown that the broad epitaxy exhibited by these films approaches single crystal behaviour to some extent.

References

[1] W. D. Nix, Met Trans. A **20A** 2217 (1989).

[2] M. J. Kobrinsky, C. V. Thompson, Acta Mater. **48** 625 (2000).

[3] G. Dehm, T. J. Balk, H. Edongué, E. Arzt, Microelectr. Eng. **70** 412 (2003).

[4] T. J. Balk, G. Dehm, E. Arzt, Acta Mater. **51** 221 (2005).

[5] P. Wellner, G. Dehm, O. Kraft, E. Arzt, Z. Metallkd. **95** 769 (2004).

[6] E. O. Hall, Proc. Roy Soc. Lon. **B64** 747 (1951).

[7] N. J. Petch, Iron Steel Inst. **174** 25 (1953).

[8] author book **113** 617 (2001).

[9] P. A. Flinn, D. S. Gardner, W. D. Nix, IEEE Trans. Elect. Dev. **34** 689 (1987).

[10] M. Ohring, Materials Science of Thin Films (Second Edition). Academic Press p735 (2002).

[11] L. B. Freund, J. Appl. Mech. **54** 553 (1987).

[12] H Gao, L. Zhang, W.D. Nix, C. V. Thompson, E. Arzt, Acta Mater. **47** 2865 (1999).

[13] D. Weiss, H. Gao, E. Arzt, Acta Mater. **49** 2395 (2001).

[14] K. H. Westmacott, S. Hinderberger, U. Dahmen, Phil. Mag. A. **81** 1547 (2001).

[15] C. V. Thompson, R. Carel, J. Mech. Phys Solids. **44** 657 (1996).

[16] P. Sonnweber-Ribic, P. Gruber, G. Dehm, E. Arzt, Acta Mater. **54** 3863 (2006).

[17] W.W. Mullins, Acta Metall. **6** 414 (1958).

[18] author book page (year).

[19] H. A. Atwater, C. V. Thompson, H. I. Smith, J. Appl. Phys. **64** 2337 (1988).

[20] H. A. Atwater, C. V. Thompson, H. I. Smith, Phys. Rev. Lett. **60** 112 (1988).

[21] G. G. Stoney, Proc. Roy. Soc. **A82** 172 (1909).

[22] B. von Blanckenhagen, P. Gumbsch, E. Arzt, Phil. Mag. Lett. **83** 1 (2001).

[23] M. J. Kobrinsky, G. Dehm, C. V. Thompson, E. Arzt, Acta Mater. **49** 3597 (2001).

[24] G. Dehm, B. J. Inkson, T. Wagner, T.J. Balk, E. Arzt, J. Mat. Sci. Techn. **18** 113 (2002).

[25] E. Eiper, J. Keckes, K. Martinschitz, I. Zizak, M. Cabié, G. Dehm, Acta Mater. **55** 1941 (2007).

[26] P. Wellner. Thermo-Mechanical Behaviour of NiAl Thin Films, Dissertation. Universität Stuttgart p. 65(2003).

[27] L. B. Adams, Mater. Ultramicroscopy **67** 11 (1997).

[28] R. Spolenak, M. T. P. Prado, Scripta Mater. **55** 103 (2006).

[29] C. B. Carter, S. M. Holmes, Phil. Mag. **35** 1161 (1977).

[30] C. J. Gallagher, Metall. Trans. **1** 2429 (1970).

[31] V. Yamakov, D. Wolf, S. R. Phillpot, A. K. Mukherjee, H. Gleiter, Nature Mater. **1** 45 (2002).

[32] L. Sauter, T. J. Balk, G. Dehm, J. Nucci, E. Arzt, Mater. Res. Soc. Symp. Proc. **875** O5.2.1 (2005).

Appendix

A TEM Sample Preparation

In order to produce the samples for *in situ* thermal cycling the following procedure was used to make discs of radius $3mm$ the centres of which were electron-transparent and unperforated.

- $3mm$ discs were cut from the wafer using an ultrasonic drill.
- The film surface was protected and the silicon substrate was ground down to around $100\mu m$.
- The Si substrate was dimple-ground until $\sim 20\mu m$ of material remained in the centre.
- A polishing wheel was then used to dimple the samples until the centre of the dimple was translucent, a thickness of around $15\mu m$.

- The samples were then etched form the reverse with a HNO_3:HF:Acetic acid mix in the ratio 2:1:1, this etches the Si and SiO_x but not the SiN_x.
- The protective layer on the Ni was carefully removed with solvent.

This procedure was only carried out for the $200nm$ films as thicker films would not be electron-transparent with the microscope available.

B Experimental errors in wafer curvature measurement

In dealing with the errors introduced through laser measurement of wafer curvature we are primarily concerned with the errors relating to the film thickness, h_f, the substrate thickness, h_s and the change in substrate curvature due to film stresses, ΔK. This leads on from the Stoney equation used to calculate the film stress [21]:

$$\sigma_f = \frac{M_s h_s^2}{6h_f}\Delta K \tag{14}$$

$$\sigma_f = \frac{M_s h_s^2}{6h_f}\left(\frac{1}{R_{meas}} - \frac{1}{R_{ref}}\right) \tag{15}$$

Here R_{meas} refers to the radius of curvature measured after film deposition and during thermal cycling while R_{ref} is the curvature of the substrate prior to film deposition. In these relations σ_f is the film stress and M_s is the biaxial elastic modulus of the substrate. Using this relation an expression for the total error in the film stress, $\Delta\sigma_f$, is as follows:

$$\Delta\sigma_f = \left|\frac{\partial\sigma_f}{\partial h_s}\right|\Delta h_s + \left|\frac{\partial\sigma_f}{\partial h_f}\right|\Delta h_f + \left|\frac{\partial\sigma_f}{\partial R_{meas}}\right|\Delta R_{meas} + \left|\frac{\partial\sigma_f}{\partial R_{ref}}\right|\Delta R_{ref} \tag{16}$$

$$\Delta\sigma_f = |\sigma_f|\,2\frac{\Delta h_s}{h_s} + |\sigma_f|\,\frac{\Delta h_f}{h_f} + \left|\frac{M_s}{6}\frac{h_s^2}{h_f}\frac{1}{R_{meas}}\right|\frac{\Delta R_{meas}}{R_{meas}} + \left|\frac{M_s}{6}\frac{h_s^2}{h_f}\frac{1}{R_{ref}}\right|\frac{\Delta R_{ref}}{R_{ref}} \tag{17}$$

Here the Δ prefix indicates the absolute error in this variable.

The substrate thickness was measured at various points and found to vary by, at most, $\pm 5\mu m$ over the whole $50mm$ wafer. For a nominal substrate thickness of $200\mu m$ this absolute error becomes a percentage error of 2.5%. The error in the film thickness is due to uncertainties in the film deposition process and is assumed to be 5%.

The most significant source of error in the stress measurement is found in the substrate curvature data. There are in fact several separate problems impacting this; the first of these being the non-uniform curvature of the substrates. In the experimental set-up used here the substrate curvature is measured along one line and averaged, this value varies somewhat for different alignments of the substrate. Care is taken experimentally to always align the substrates the same way but this does not completely eliminate the error. In order to quantify this error the curvature of several wafers was measured and then remeasured following removal and remounting of the wafer. This returned an error of 10% in both R_{meas} and R_{ref}. The second source of error arises from the accuracy with which the laser measures the radii of curvature, this error is negligible in comparison to the other

experimental errors and hence can be neglected. The final source of error in the curvature measurement comes about due to thermal drift of the wafer during heating. Unfortunately it is very difficult to accurately quantify the error introduced through this drift, it should be noted however that this will always lead to larger errors at elevated temperatures as the drift moves the wafer away from the initial position.

These values can then be inserted into equation 18 such that the relation below is produced:

$$\Delta\sigma_f = 0.10\,|\sigma_f| + 0.20\left|\frac{M_s}{6}\frac{h_s^2}{h_f}\frac{1}{R_{ref}}\right| \tag{18}$$

Here the separate 10% errors in R_{meas} and R_{ref} have been combined for simplicity to give $\Delta R_{ref}/R_{ref} = 20\%$. It can be seen from this relation that, for a given substrate and film thickness, the error is smaller when the radius of curvature of the wafer is large.

C Microstructural Data

C.1 Representative FIB micrographs

Presented here are FIB (FEI 200 at $30kV$) micrographs representative of those captured in several areas of the film surface. In addition to this an image of a trench cut through the film is presented. These trenches allow the 3D nature of the films to be estimated, in this case all the films appear to be fully columnar.

C.1.1 $1000nm$ film on SiN_x/SiO_x

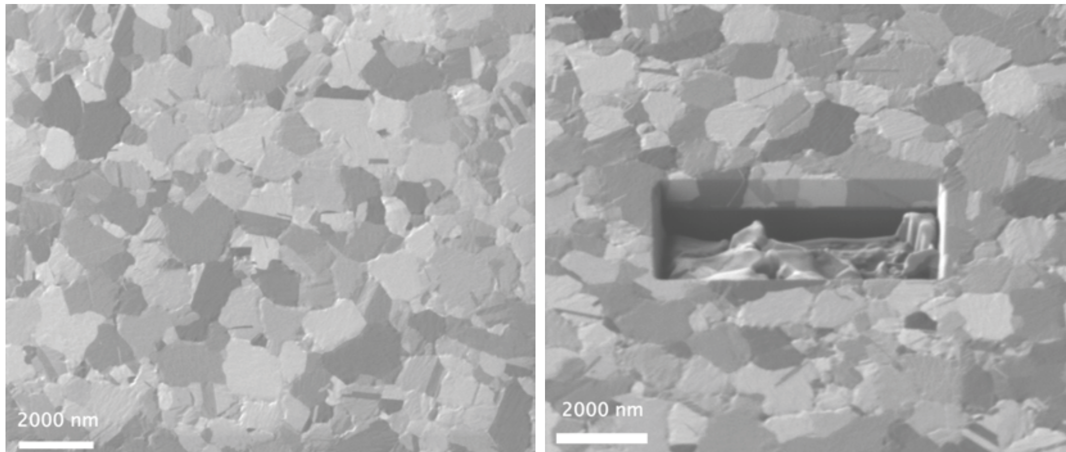

Figure 29: FIB micrographs of the $1000nm$ Ni film on SiN_x/SiO_x; a) general microstructure at $20kX$ magnification, b) FIB trench showing cross-section at $25kX$.

C.1.2 $600nm$ film on SiN_x/SiO_x

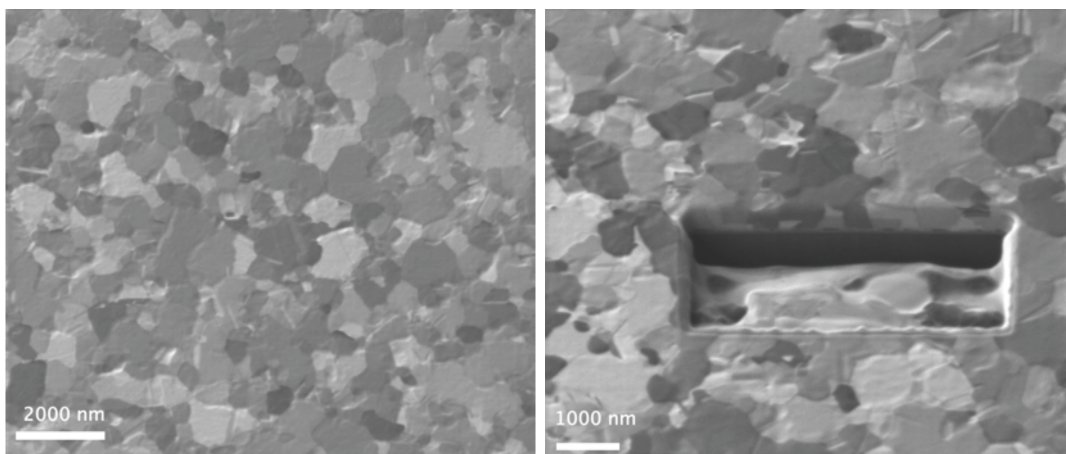

Figure 30: FIB micrographs of the $600nm$ Ni film on SiN_x/SiO_x; a) general microstructure at $25kX$ magnification, b) FIB trench showing cross-section at $35kX$.

C.1.3 $400nm$ film on SiN_x/SiO_x

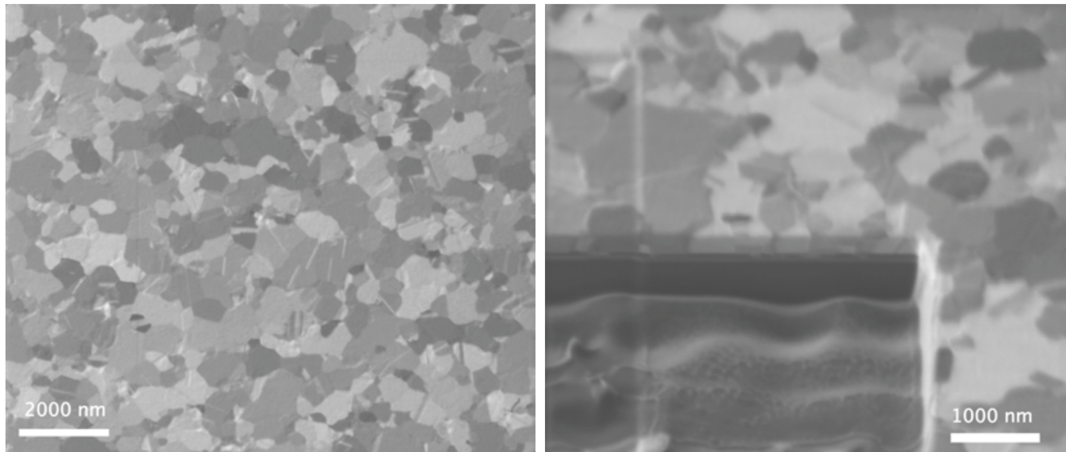

Figure 31: FIB micrographs of the $400nm$ Ni film on SiN_x/SiO_x; a) general microstructure at $35kX$ magnification, b) FIB trench showing cross-section at $50kX$.

C.1.4 $200nm$ film on SiN_x/SiO_x

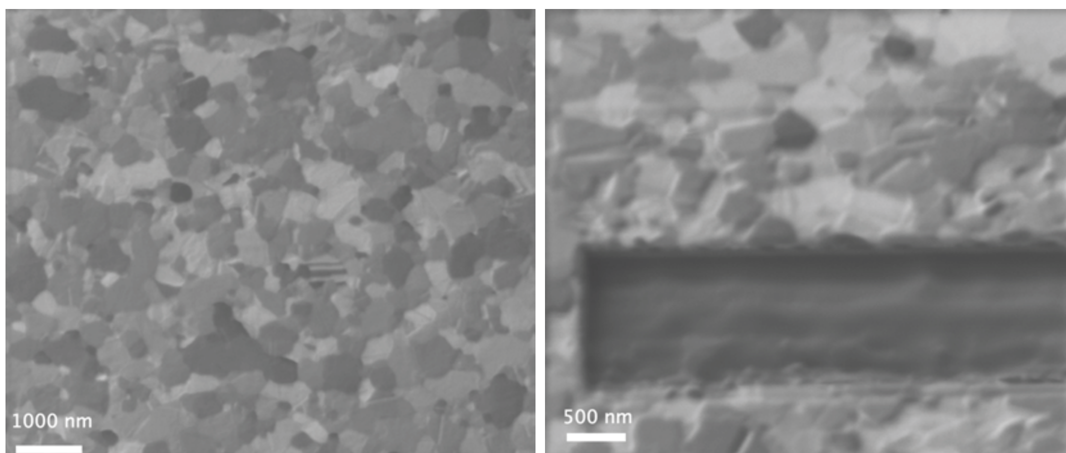

Figure 32: FIB micrographs of the $200nm$ Ni film on SiN_x/SiO_x; a) general microstructure at $35kX$ magnification, b) FIB trench showing cross-section at $65kX$.

C.1.5 150nm film on SiN_x/SiO_x

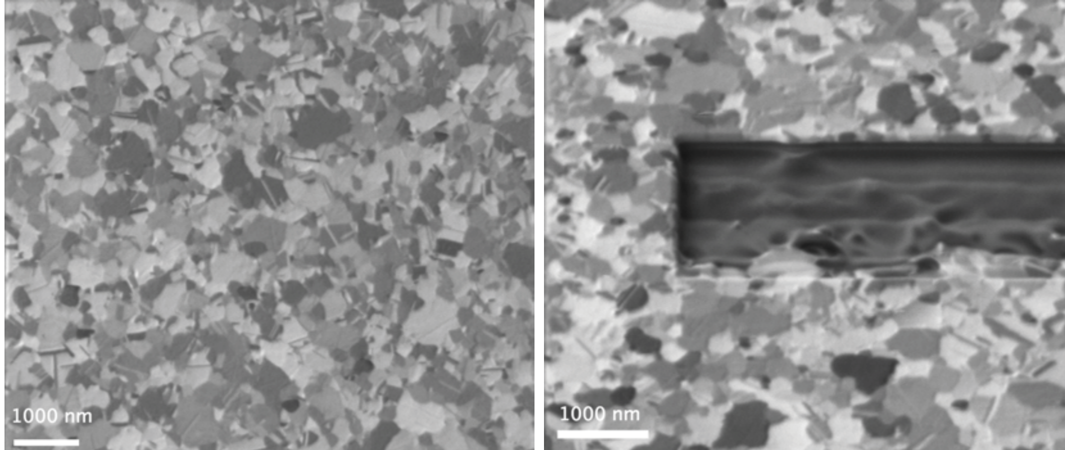

Figure 33: FIB micrographs of the 150nm Ni film on SiN_x/SiO_x; a) general microstructure at 35kX magnification, b) FIB trench showing cross-section at 50kX.

C.2 Grain count statistics

Using FIB micrographs similar to those presented above the individual grain boundaries were outlined onto an overlaying sheet of acetate, straight boundaries indicative of annealing twins were ignored in this process. These sheets of acetate were then used in conjunction with an image analysis apparatus (Leica, Quantimet Q500/W) to assess the area of the grains. This software then converted these grain areas into grain diameters for circles of equal area. The population distribution of these grain diameters for each of the films on Si substrates is presented below.

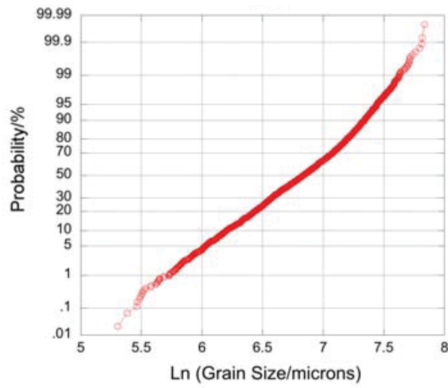

(a) $1000nm$

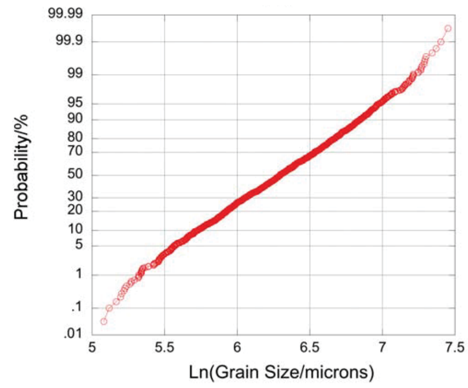

(b) $600nm$

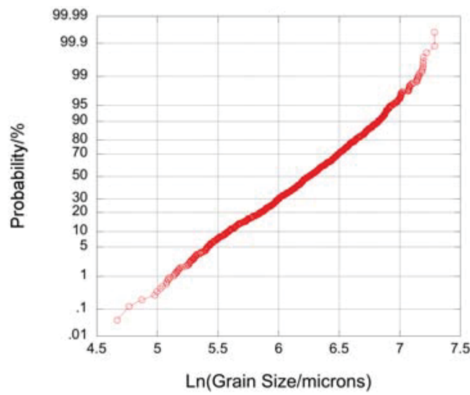

(c) $400nm$

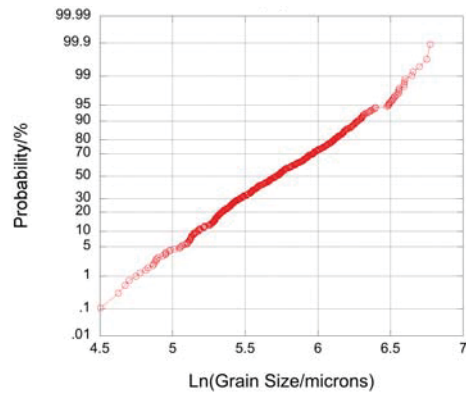

(d) $200nm$ FIB

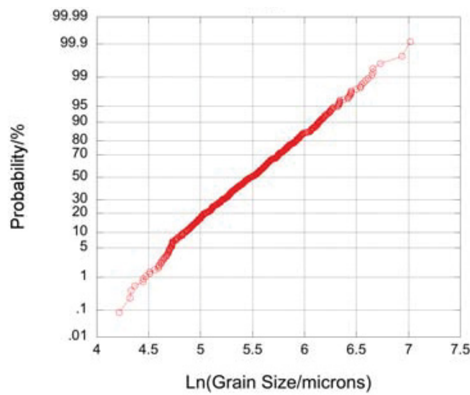

(e) $200nm$ TEM

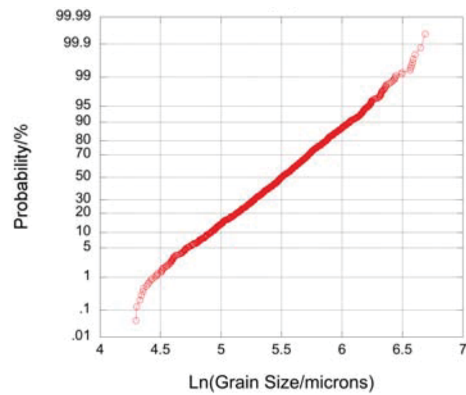

(f) $150nm$

Figure 34: Probability plots for the Ni films on SiN_x/SiO_x plotted against the natural logarithm of the grain size. The high degree of linearity observed here indicates a log-normal distribution of grain size.

C.3 EBSD Data

The microstructure of the epitaxial Ni films on α-Al_2O_3 substrates was assessed with EBSD (LEO 1525 SEM, EDAX camera). Using this technique the local crystallographic alignment of the Ni is assessed at $2\mu m$ intervals over the film surface. This data is then converted into various types of plot by the software provided, please see section 3.2 for details of the different plots. All plots are for the same film area.

C.3.1 $1000nm$ film on α-Al_2O_3

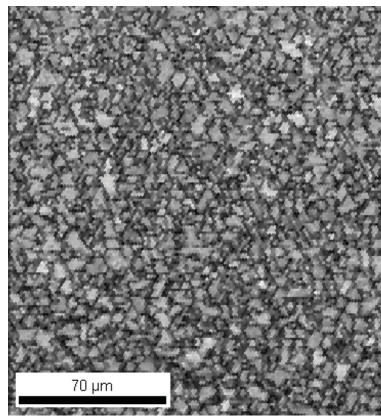

(a) IQ Plot

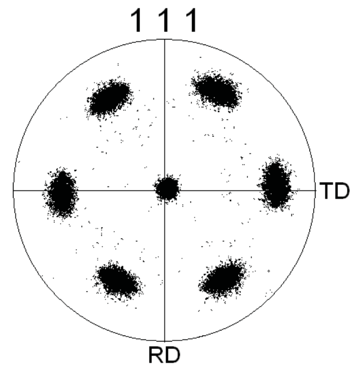

(b) Pole Figure

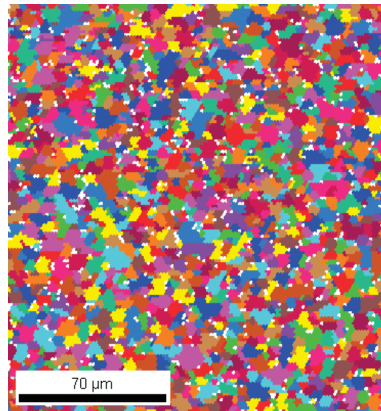

(c) 1° misorientation unique grains

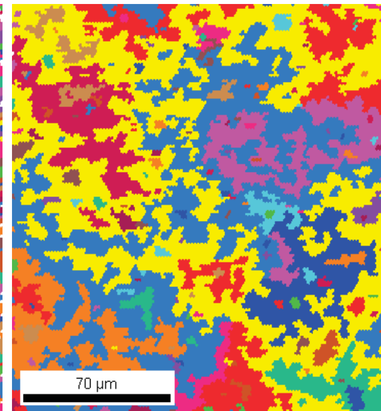

(d) 15° misorientation unique grains

Figure 35: EBSD data for the $1000nm$ epitaxial Ni film

C.3.2 600nm film on α-Al_2O_3

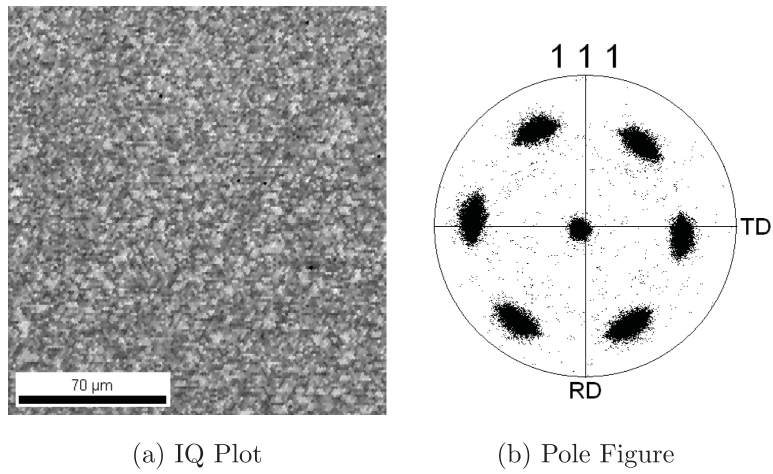

(a) IQ Plot (b) Pole Figure

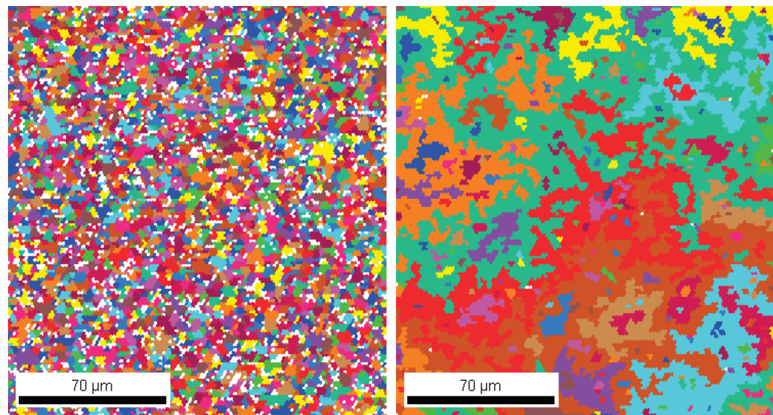

(c) 1° misorientation unique grains (d) 15° misorientation unique grains

Figure 36: EBSD data for the 600nm epitaxial Ni film

C.3.3 400nm film on α-Al_2O_3

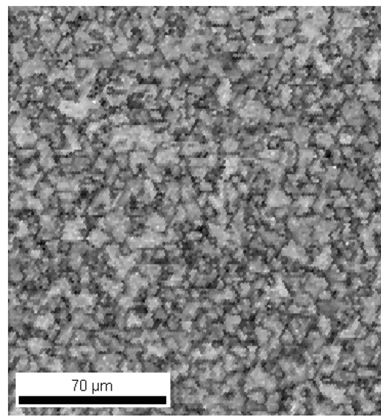

(a) IQ Plot

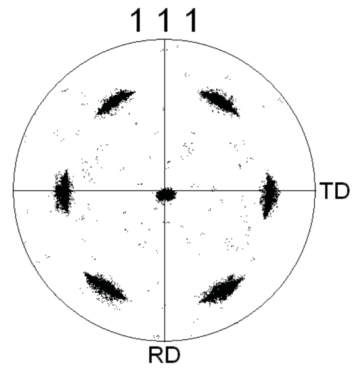

(b) Pole Figure

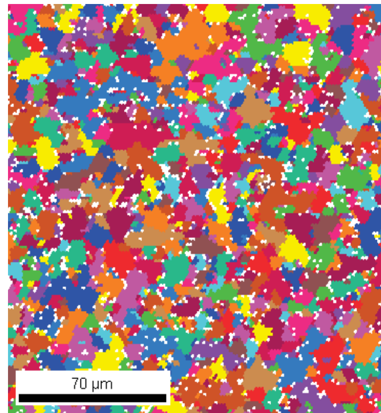

(c) 1° misorientation unique grains

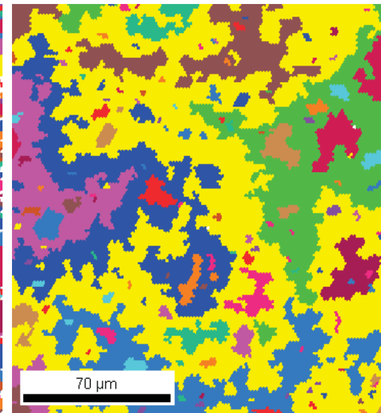

(d) 15° misorientation unique grains

Figure 37: EBSD data for the 400nm epitaxial Ni film

C.3.4 $200nm$ film on α-Al_2O_3

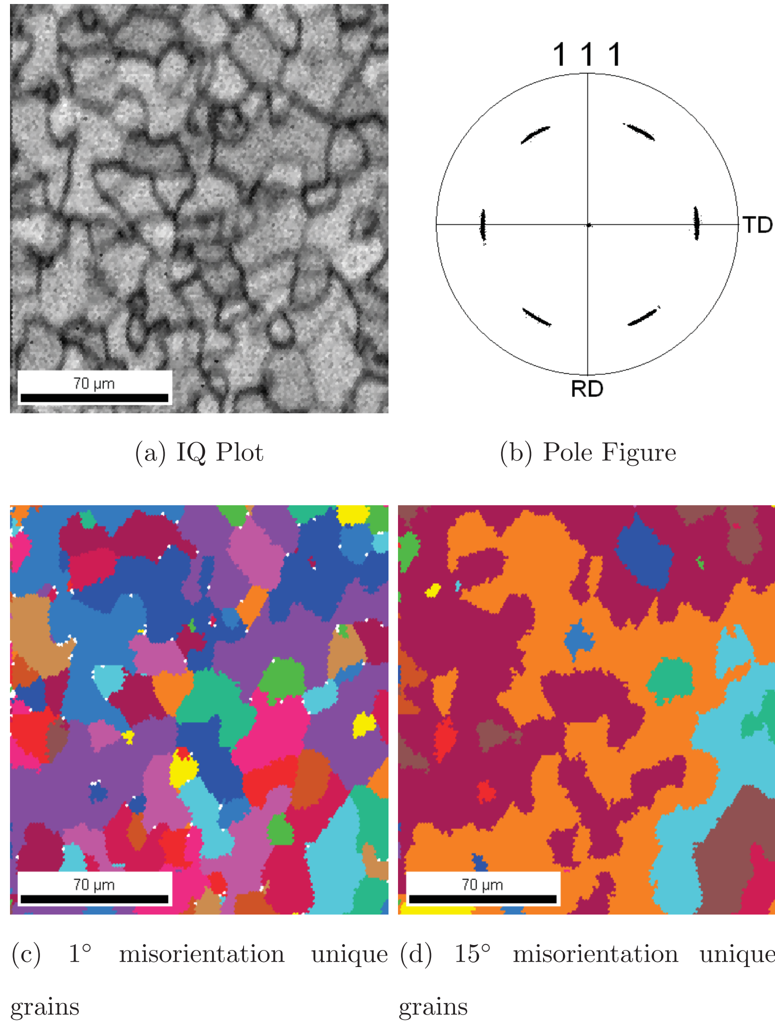

(a) IQ Plot

(b) Pole Figure

(c) 1° misorientation unique grains

(d) 15° misorientation unique grains

Figure 38: EBSD data for the $200nm$ epitaxial Ni film

D Wafer curvature data

Presented here is all the wafer curvature data collected for the Ni films on both SiN_x/SiO_x and α-Al_2O_3 substrates. Where data points are missing the apparatus lost the signal from the laser and an erroneous curvature was recorded.

D.1 Polycrystalline Films

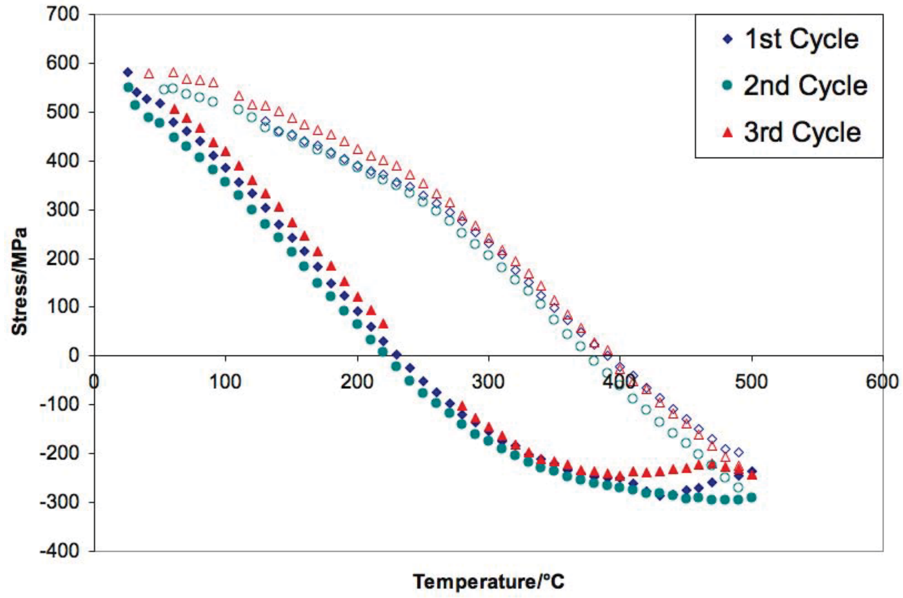

Figure 39: Wafer curvature data for the 1000nm Ni film on SiN_x/SiO_x.

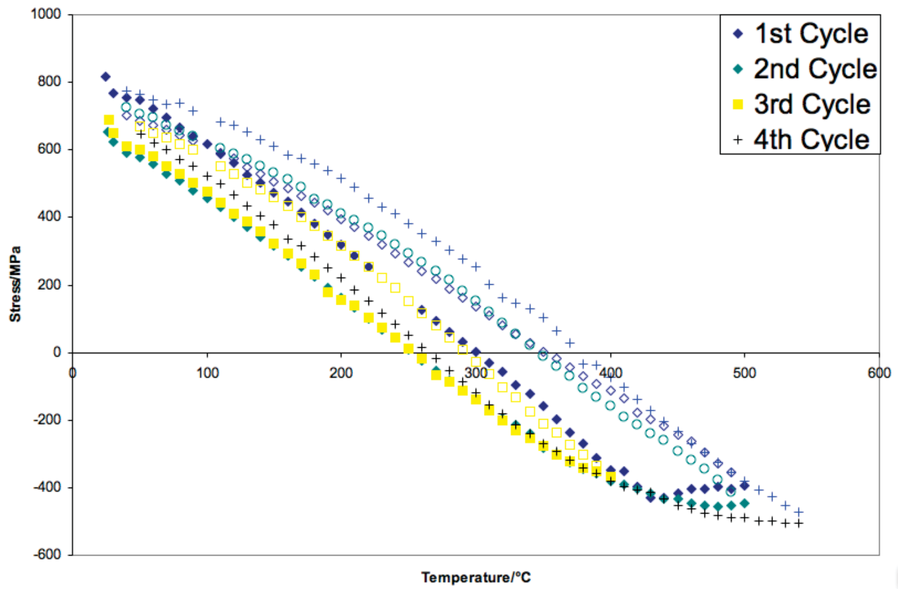

Figure 40: Wafer curvature data for the 600nm Ni film on SiN_x/SiO_x.

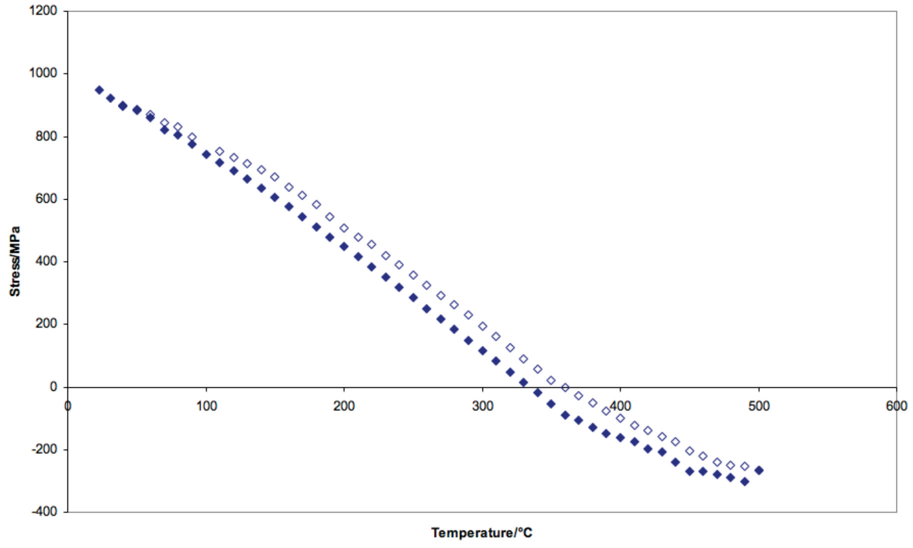

Figure 41: Wafer curvature data for the 400nm Ni film on SiN_x/SiO_x.

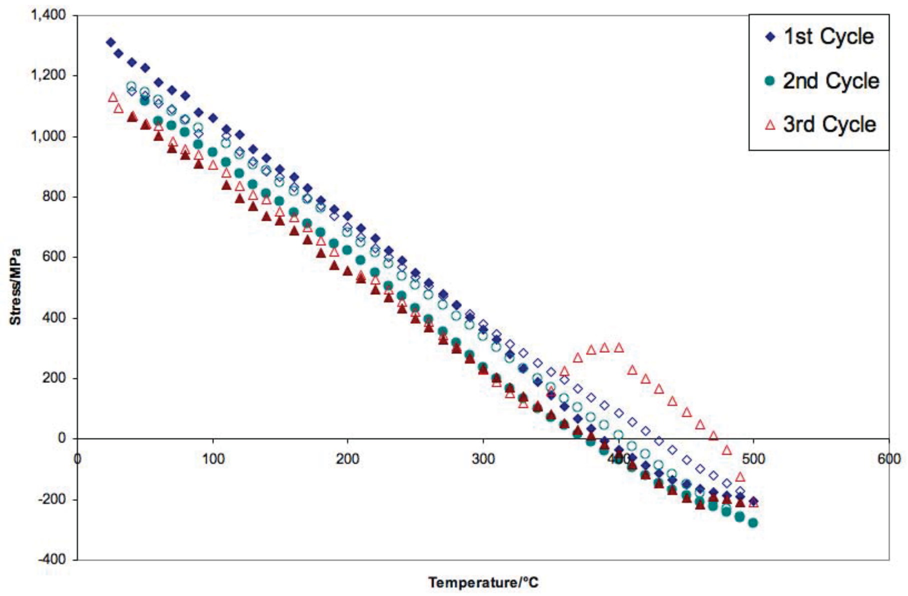

Figure 42: Wafer curvature data for the 200nm Ni film on SiN_x/SiO_x.

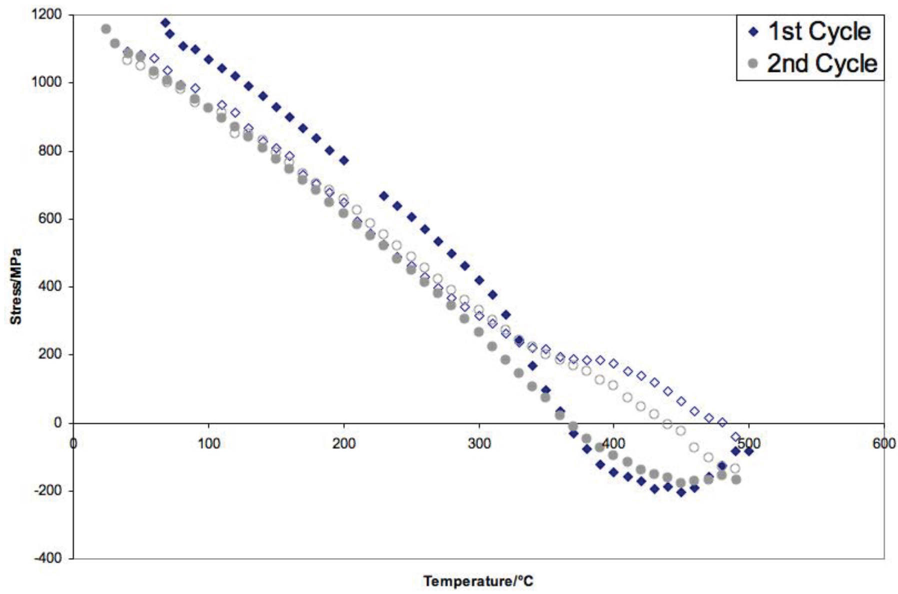

Figure 43: Wafer curvature data for the 150nm Ni film on SiN_x/SiO_x.

D.2 Epitaxial Films

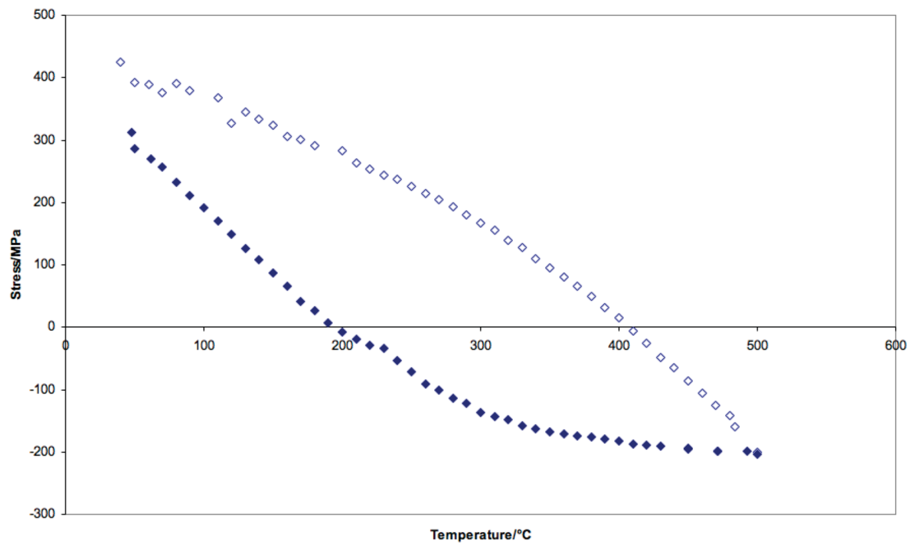

Figure 44: Wafer curvature data for the 1000nm Ni film on α-Al_2O_3.

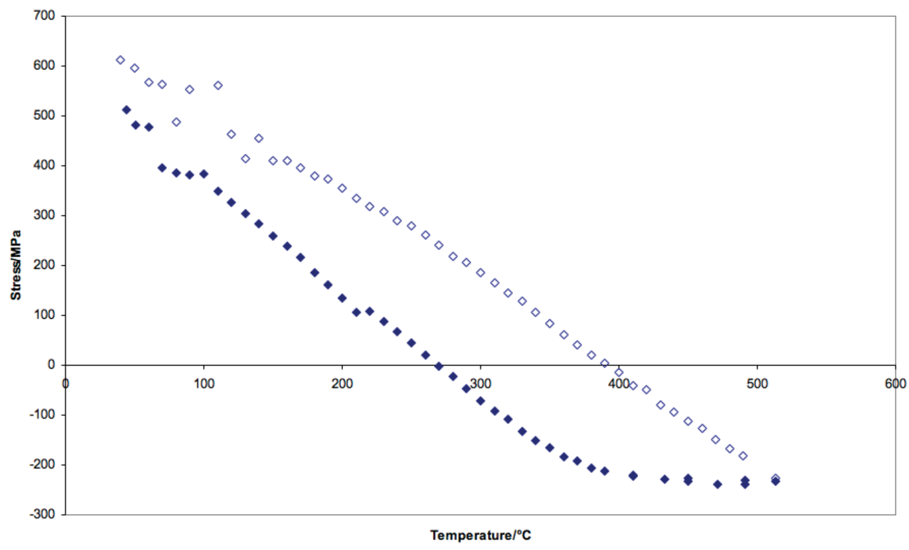

Figure 45: Wafer curvature data for the 600nm Ni film on α-Al_2O_3.

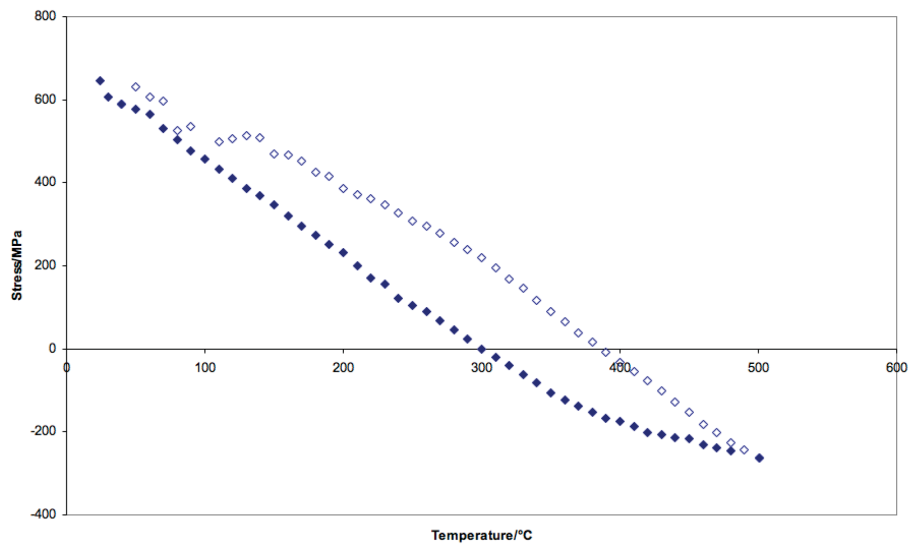

Figure 46: Wafer curvature data for the 400nm Ni film on α-Al_2O_3.

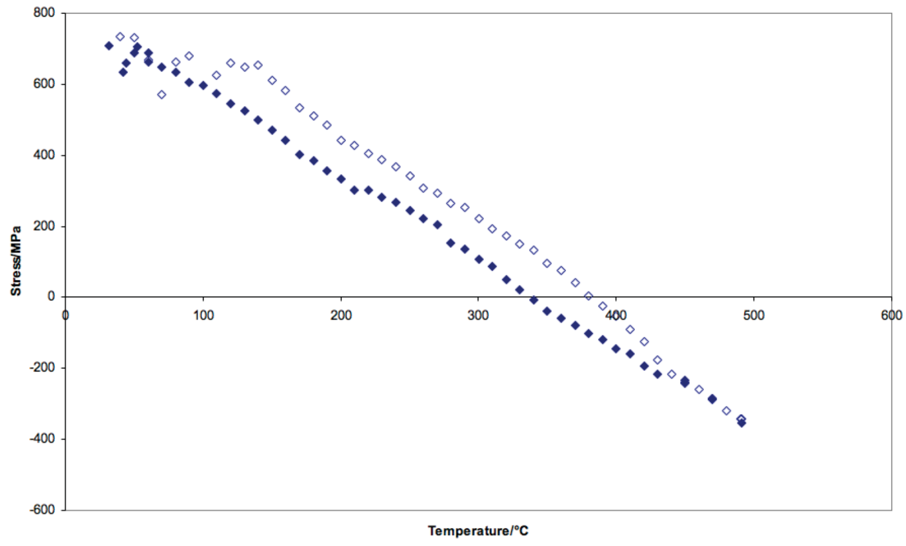

Figure 47: Wafer curvature data for the 200nm Ni film on α-Al_2O_3.